The Astrophysical Journal, 891:66 (18pp), 2020 March 1 https://doi.org/10.3847/1538-4357/ab700a

Large-scale Molecular Gas Distribution in the M17 Cloud Complex: Dense Gas Conditions of Massive Star Formation?

Quang Nguyen-Luong[1,2], Fumitaka Nakamura[3,4,5], Koji Sugitani[2], Tomomi Shimoikura[6], Kazuhito Dobashi[7], Shinichi W. Kinoshita[3,4], Kee-Tae Kim[8,9], Hynwoo Kang[8], Patricio Sanhueza[3], Neal J. Evans II[8,10], and Glenn J. White[11,12]
[1] McMaster University, 1 James St N, Hamilton, ON, L8P 1A2, Canada; nguyeq12@mcmaster.ca
[2] Graduate School of Natural Sciences, Nagoya City University, Mizuho-ku, Nagoya, Aichi 467-8601, Japan
[3] National Astronomical Observatory of Japan, 2-21-1 Osawa, Mitaka, Tokyo 181-8588, Japan
[4] Department of Astronomy, The University of Tokyo, Hongo, Tokyo 113-0033, Japan
[5] The Graduate University for Advanced Studies (SOKENDAI), 2-21-1 Osawa, Mitaka, Tokyo 181-0015, Japan
[6] Faculty of Social Information Studies, Otsuma Women's University, Chiyoda-ku,Tokyo, 102-8357, Japan
[7] Department of Astronomy and Earth Sciences, Tokyo Gakugei University, 4-1-1 Nukuikitamachi, Koganei, Tokyo 184-8501, Japan
[8] Korea Astronomy & Space Science Institute, 776 Daedeokdae-ro, Yuseong-gu, Daejeon 34055, Republic of Korea
[9] University of Science and Technology, Korea (UST), 217 Gajeong-ro, Yuseong-gu, Daejeon 34113, Republic of Korea
[10] Department of Astronomy, The University of Texas at Austin, 2515 Speedway, Stop C1400, Austin, TX 78712-1205, USA
[11] Department of Physics and Astronomy, The Open University, Walton Hall, Milton Keynes, MK7 6AA, UK
[12] RAL Space, STFC Rutherford Appleton Laboratory, Chilton, Didcot, Oxfordshire, OX11 0QX, UK
Received 2019 October 24; revised 2020 January 15; accepted 2020 January 24; published 2020 March 4

Abstract

The non-uniform distribution of gas and protostars in molecular clouds is caused by combinations of various physical processes that are difficult to separate. We explore this non-uniform distribution in the M17 molecular cloud complex that hosts massive star formation activity using the ^{12}CO ($J = 1$–0) and ^{13}CO ($J = 1$–0) emission lines obtained with the Nobeyama 45 m telescope. Differences in clump properties such as mass, size, and gravitational boundedness reflect the different evolutionary stages of the M17-H II and M17-IRDC clouds. Clumps in the M17-H II cloud are denser, more compact, and more gravitationally bound than those in M17-IRDC. While M17-H II hosts a large fraction of very dense gas (27%) that has a column density larger than the threshold of $\sim$1 g cm^{-2} theoretically predicted for massive star formation, this very dense gas is deficient in M17-IRDC (0.46%). Our HCO^+ ($J = 1$–0) and HCN ($J = 1$–0) observations with the Taeduk Radio Astronomy Observatory 14 m telescope trace all gas with a column density higher than 3×10^{22} cm^{-2}, confirming the deficiency of high-density ($\gtrsim 10^5$ cm^{-3}) gas in M17-IRDC. Although M17-IRDC is massive enough to potentially form massive stars, its deficiency of very dense gas and gravitationally bound clumps can explain the current lack of massive star formation.

Unified Astronomy Thesaurus concepts: Star formation (1569); Giant molecular clouds (653); Diffuse molecular clouds (381); Interstellar medium (847); Protostars (1302)

1. Introduction

The discovery of carbon monoxide (CO) in the interstellar medium opened a new window into the molecular gas universe (Wilson et al. 1970). Understanding how molecular gas is organized into structures is important because it has an essential role in nurturing the star and planet formation processes. In addition to a degree-resolution all-sky area in CO ($J = 1$–0) (Dame et al. 2001), numerous higher-resolution wide-field CO surveys have presented three-dimensional (3D) space space–velocity structures of the molecular gas environments in more detail (e.g., Schneider et al. 2010; Carlhoff et al. 2013; Dempsey et al. 2013; Barnes et al. 2015). Wide-field mapping of denser gas tracers, i.e., HCO^+, HCN, CS, also probe into the inner dense region of the molecular clouds (Wu et al. 2010; Kauffmann et al. 2017; Pety et al. 2017).

Using one of the world's largest millimeter-waveband telescopes, the 45 m telescope of the Nobeyama Radio Observatory (NRO 45 m), we have conducted a high spatial resolution, highly sensitive, large-dynamical-range wide-field survey of CO ($J = 1$–0) and other gases to explore the molecular cloud structure in both low-mass and high-mass star-forming regions. The project is named the "Star Formation Legacy project" and presented in Nakamura et al. (2019a). The detailed observational results for the individual regions are given in other articles (Orion A: Ishii et al. 2019; Nakamura et al. 2019b; Tanabe et al. 2019; M17: Shimoikura et al. 2019a; Sugitani et al. 2019; Aquila Rift: Shimoikura et al. 2019b; Kusune et al. 2019; other regions: Dobashi et al. 2019a, 2019b).

As a part of the project, we investigate the global molecular gas distribution of the M17 region to understand the role of dense gas in star formation in M17 (see Figure 1 for the wide-field infrared and submillimeter image of the mapped region). The ^{12}CO ($J = 1$–0) and ^{13}CO ($J = 1$–0) data from the NRO 45 m telescope is complemented by HCN ($J = 1$–0) and HCO^+ ($J = 1$–0) observed by the Taeduk Radio Astronomy Observatory (TRAO) 14 m telescope. We provide an overview of the M17 complex in Section 2. Section 3 describes the detailed observations and data used in this paper. The global structure of molecular gas and dense gas is examined in Section 4 and the role of dense gas in star formation in M17 is discussed in Section 5. Finally, we summarize the results in Section 6.

2. Overview of the M17 Region

The M17 complex is a $\sim 2^\circ \times 2^\circ$ molecular cloud complex surrounding the M17 nebula (also called The Omega, or The Horseshoe, or The Swan nebula) and is located in the Sagittarius spiral arm (Elmegreen et al. 1979; Reid et al. 2019).

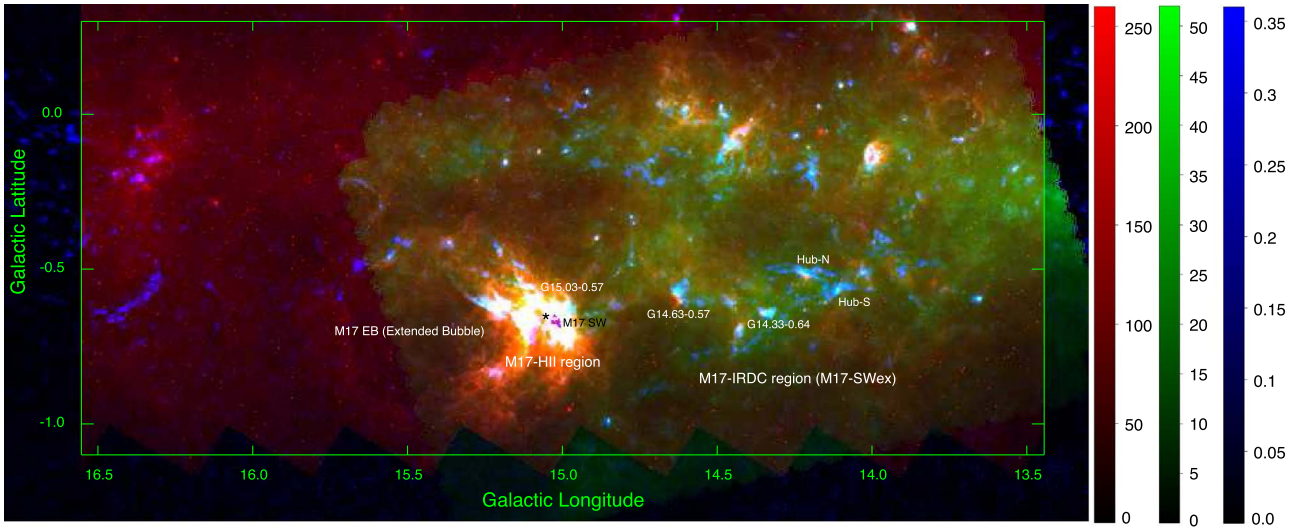

Figure 1. Three-color image of the M17 region as seen at 24 μm in MJy sr^{-1} (red, *Spitzer*), 250 μm in Jy beam^{-1} (green, *Herschel*), and 870 μm in Jy beam^{-1} (*blue*, APEX).

The M17 nebula is excited by the 1 Myr-old NGC 6618 loose (radius >1 pc) open cluster, which contains hundreds of stars with spectral types earlier than B9 (Lada et al. 1991). The Massive Young Star-forming Complex Study in IR and X-ray (MYStIX) survey with the *Chandra* X-Ray Observatory counted a total of 16,000 stars in the NGC 6618 (M17) cluster (Kuhn et al. 2015). It is the second most populated cluster after the Carina cluster in the MYStIX survey (Kuhn et al. 2015). For comparison, while NGC 6611 and the Orion Nebula Cluster have peak stellar surface densities of around 10–100 stars pc^{-2}, that of NGC 6618 is remarkably much higher, >1000 stars pc^{-2}. The H II region (M17-H II region) surrounding the cluster has opened a large gap at its edge, which lets stellar radiation and winds escape exciting a diffuse X-Ray emitting region observed with the *Chandra* Observatory (Townsley et al. 2003). In addition to the relatively mature H II region around the cluster, other notable star-forming regions have been discovered in the vicinity of M17, such as the immediate environment of M17 (Ando et al. 2002), or the M17 Infrared Dark Cloud (M17-IRDC, also known as M7-SWex), which contains the IRDC G14.225-0.506 (Povich & Whitney 2010; Ohashi et al. 2016; Povich et al. 2016). IRDCs are molecular clouds known to host the earliest stages of high-mass star formation (e.g., Sanhueza et al 2019). M17 forms a larger molecular cloud complex together with the M16 cloud, as suggested by Nguyen-Luong et al. (2016).

Parallax distances of $1.83^{+0.08}_{-0.07}$ kpc and $1.98^{+0.14}_{-0.12}$ kpc by maser monitoring have been determined toward two dust clumps in M17, G014.63-00.57 and G015.03-00.57, respectively (Honma et al. 2012; Wu et al. 2014). These parallax distances are larger than photometric distances of 1.3 $\pm$ 0.4 kpc (Hanson et al. 1997) and 1.6 $\pm$ 0.3 kpc (Nielbock et al. 2001), obtained by the analysis of the main-sequence OB stars. Note that Chini et al. (1980) derived a distance of 2.2 kpc to M17 based on the multi-color photometry. Other parallax measurements to M17-H II region have suggested a distance of 2.0 kpc (Xu et al. 2011), 1.9 $\pm$ 0.1 kpc (Wu et al. 2019), or $2.04^{+0.16}_{-0.17}$ kpc (Chibueze et al. 2016). To be consistent with other papers in our project (Shimoikura et al. 2019a; Sugitani et al. 2019), we adopt 2 kpc to be the distance to the entire M17 complex.

Elmegreen et al. (1979) found a velocity gradient in the M17 molecular cloud complex from northeast to southwest based on the low-resolution ^{12}CO (J = 1–0) and ^{13}CO (J = 1–0) observations. They suggested that the gradient may be an outcome of the recent passage of a Galactic spiral density wave, which has triggered star formation in M17. The spiral density waves compress the interstellar gas, promoting the formation of giant molecular clouds. The spiral density waves also enhance the collision rates of molecular clouds, which can trigger massive star formation and star cluster formation efficiently (Scoville et al. 1986; Tan 2000; Nakamura et al. 2012; Fukui et al. 2014; Wu et al. 2017; Dobashi et al. 2019b). In fact, Nishimura et al. (2018) recently found evidence for a cloud-cloud collision near the M17-H II region. However, streaming motions from the spiral waves can also inhibit massive star formation, a fact that has been seen in other galaxies such as M51 (Meidt et al. 2013). In either case, the M17 complex, as a whole, is well-suited to study the effect of dynamical compression of interstellar gas by the Galactic spiral density wave. Interestingly, a second compression at the interface of the M17-H II region when the OB star clusters compress the edge of the cloud also occurred, which can be seen in CO (J = 3–2) (Rainey et al. 1987) and also in a high-density tracer such as HCN (J = 4–3) (White et al. 1982).

From the *Spitzer* observations, Povich & Whitney (2010) and Povich et al. (2016) discovered that the mass function of young stellar objects (YSOs) around the M17-H II region seems consistent with the Salpeter initial mass function (IMF), whereas that in the M17-IRDC is significantly steeper than the Salpeter IMF. In other words, the high-mass stellar population in M17-IRDC is deficient. This fact makes the M17 region an attractive test case for models of high-mass star formation.

3. Observations

3.1. CO Observations from the NRO 45 m Star Formation Project

The data come from the NRO 45 m star formation project (PI: Fumitaka Nakamura) which observed ^{12}CO (J = 1–0), ^{13}CO (J = 1–0), C^{18}O (J = 1–0), N_2H^+ (J = 1–0) and CCS ($J_N = 8_7 - 7_6$) lines toward a sample of star-forming regions:

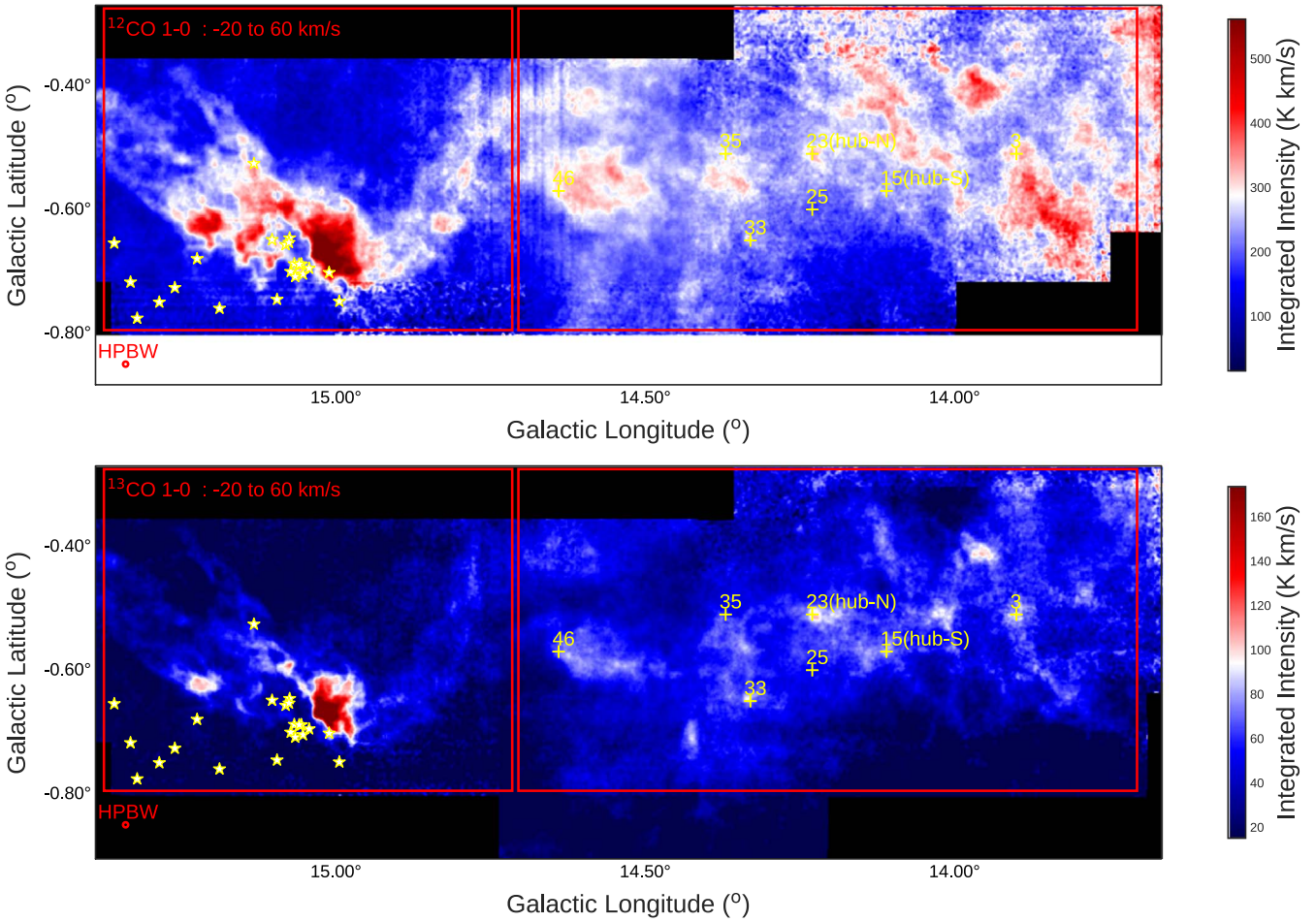

Figure 2. The M17 complex in (upper) ^{12}CO(J = 1–0) and (lower) ^{13}CO(J = 1–0) from the NRO 45 m star formation survey, integrated over the entire velocity range (from −20 to 60 km s^{-1}). The red rectangles outline the two prominent star-forming regions: M17-H II (left) and M17-IRDC (right). The star symbols pinpoint the OB star clusters responsible for the giant H II region. The cross symbols pinpoint the locations of the massive cores ($M > 500\,M_{\odot}$) reported by Shimoikura et al. (2019a).

M17, Orion, and Aquila Rift. M17 is the most distant star-forming region in the survey. We carried out the mapping observations toward M17 between December 2014 and March 2017. The three CO isotopologue lines were observed using the four-beam dual polarization, sideband-separating SIS FOREST receiver (Minamidani et al. 2016). However, the C^{18}O coverage is smaller than those of ^{12}CO and ^{13}CO, due to malfunction of a sub-reflector system in one period of observations. See Nakamura et al. (2019a) for more details of the observations.

The telescope HPBW beam size is ∼15″ and the main-beam efficiency $\eta_{\rm MB} \sim 40\%$ at 115 GHz. We used the SAM45 spectrometer as the backend, which provided a bandwidth of 63 MHz and a frequency resolution of 15.26 kHz, corresponding to a velocity resolution of ∼0.04 km s^{-1}. Standard on-the-fly (OTF) mapping techniques were used to carry out the mapping observations. Details on the observation procedure, such as OFF-positions, submapping integration time, efficiency, etc., can be found in Nakamura et al. (2019a).

The raw data were reduced by the NRO data reduction tool, NOSTAR. ^{12}CO, ^{13}CO, and C^{18}O data were convolved to 22″ beam size and reprojected to a common 7.″5 × 7.″5 grid to facilitate our analysis. Figure 2 shows the ^{12}CO and ^{13}CO intensity maps integrated from –20 to 60 km s^{-1}. The rms noise levels were calculated as the average of the emission-free channels from –18 to –11 km s^{-1}. The average rms of ^{12}CO, ^{13}CO, and C^{18}O are ∼1.0, 0.4, and 0.3 K per 7.″5-pixel and per 0.1 km s^{-1} channel, respectively (Figure 3). The data are available online.[13]

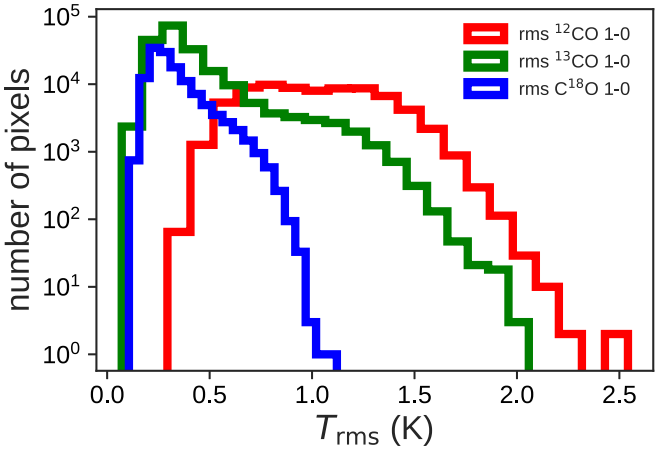

Figure 3. Histograms of the rms maps of ^{12}CO(J = 1–0) (red), ^{13}CO(J = 1–0) (green), and C^{18}O(J = 1–0) (blue) of the M17 data.

[13] http://jvo.nao.ac.jp/portal/v2/

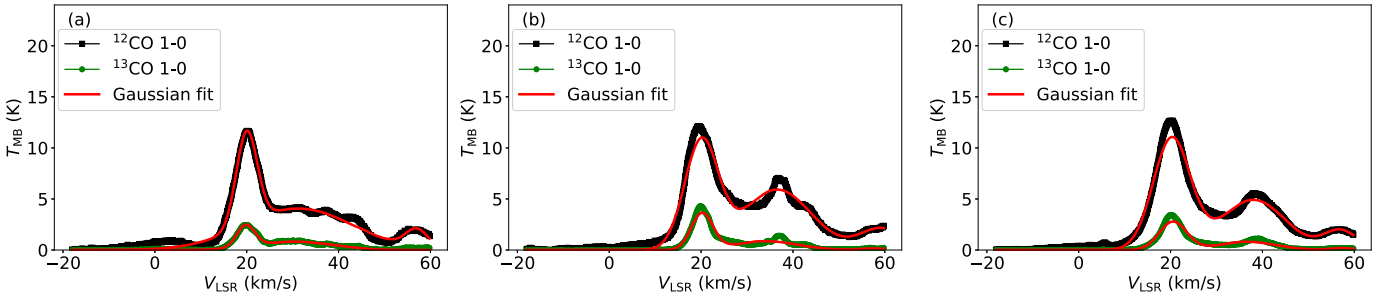

Figure 4. ^{12}CO (J = 1–0) (blue) and ^{13}CO (J = 1–0) (magenta) spectra averaged over the (a) M17-H II, (b) M17-IRDC, and (c) entire M17 regions. The red curves are three-Gaussian component models that best fit the data, and the fitted parameters are listed in Table 1.

3.2. HCO^+ and HCN Observations with TRAO 14 m Telescope

HCO^+ (J = 1–0, 89188.526 MHz) and HCN (J = 1–0, 88631.6023 MHz) lines were observed simultaneously with the TRAO 14 m telescope. The telescope was equipped with the SEQUOIA receiver with 16 pixels in 4 × 4 array. The 2nd IF modules with the narrowband and the eight channels with 4 FFT spectrometers allow observation of two frequencies simultaneously within the 85–100 or 100–115 GHz frequency ranges for all 16 pixels. We carried out the M17 observations between 2016 December and 2017 December. Observations were done in the OTF mode, and the native velocity resolution is about 0.05 km s^{-1} (15 kHz) per channel, and their full spectral bandwidth is 62.5 MHz with 4096 channels. The telescope HPBW beam size is ∼50″ at 100 GHz and the main-beam efficiency η_{MB} is ∼46% at 89 GHz. The system temperature was in the range 150–300 K. The cube was regridded to a 7.″5 × 7.″5 grid.

4. Results

4.1. Multiple Cloud Ensemble along the Line of Sight (LOS)

The ^{12}CO (J = 1–0) and ^{13}CO (J = 1–0) intensity maps integrated over the entire velocity range from −20 to 60 km s^{-1} in Figure 2 show the global molecular gas distribution of the M17 complex. The maps cover an area of 1.°72 × 0.°53 from 13.°67 to 15.°39 in Galactic longitude and from −0.°80 to −0.°27 in Galactic latitude. The CO emission around the H II region encompassing the NGC 6618 cluster stands out as the brightest subregion in the map. Also, the emission from the M17-IRDC region is notable in both ^{12}CO and ^{13}CO.

The integrated spectra of ^{12}CO and ^{13}CO toward the M17 complex show three major peaks over the complete velocity ranging from −20 to 60 km s^{-1} (see Figure 4(c)). The averaged spectra are fitted with three velocity components that show three main components peaking at ∼20 km s^{-1}, ∼38 km s^{-1}, and ∼57 km s^{-1}; velocity dispersion $\sigma = \frac{\mathrm{FWHM}}{2\sqrt{2\ln 2}}$ of ∼4.0 km s^{-1}, 6.9 km s^{-1}, and 3.7 km s^{-1}, respectively. The fitted parameters are summarized in Table 1. It seems that the main component centers around ∼20 km s^{-1} and the other two components center around ∼38 and ∼57 km s^{-1}. This becomes more obvious when comparing the ^{12}CO and ^{13}CO spectra averaged over the entire M17 complex with those of the individual regions M17-H II and M17-IRDC (Figures 4(a) and (b)). Each spectrum in these three panels shows distinct peaks at different velocities, but the dominant peak is around V_{LSR} ∼ 20 km s^{-1}, which is the main velocity peak of both M17-H II and M17-IRDC regions (Elmegreen et al. 1979). In the average spectrum, we can find at least four groups of molecular clouds in the LSR velocity ranges <10, 10–30, 30–50, and >50 km s^{-1}.

We further examine the distances of dense clumps in M17 detected with ATLASGAL survey (Schuller et al. 2010; Csengeri et al. 2017). The distances were measured by Wienen et al. (2015) and Urquhart et al. (2018) using the kinematic method and cross-correlating with maser parallax measurements if available to resolve the distance ambiguity issues. Approximately 90% of sources have distances of 1.8 or 1.9 kpc (Figure 5), which implies that most clumps in the M17 region are located around 1.9 ± 0.1 kpc and the region might have a depth of ∼0.1–0.3 kpc. The distances of dense clumps are close to our assumption of 2 kpc. The ^{12}CO and ^{13}CO position–velocity diagrams show that the emission lines smoothly change from M17-H II and M17-IRDC in terms of the radial velocity, line width, and intensity, indicating that the two subregions are physically connected (Shimoikura et al. 2019a). Thus, the assumption that the two subregions are located at the same distance ∼2 kpc is justifiable.

In the Appendix (Figures 18 and 19), we show the ^{12}CO and ^{13}CO (J = 1–0) intensity maps, respectively, integrated over the velocity ranges from −20 to 10 km s^{-1}, 10 to 30 km s^{-1}, 30 to 50 km s^{-1}, and 50 to 60 km s^{-1}. The bulk of the M17 emission is seen in the velocity range 10–30 km s^{-1} in both ^{12}CO and ^{13}CO (J = 1–0) lines. M17-H II region is especially bright in the ^{12}CO (J = 1–0) maps and the M17-IRDC region is more prominent in ^{13}CO (J = 1–0). The emission in the range 30–50 km s^{-1} is stronger toward the Galactic equator and distributed over a larger region on the plane of the sky. The BeSSeL parallax-Based Distance Calculator confirmed that the main velocity component 10–30 km s^{-1} is more likely to be in the Sagittarius arm, whereas the 30–50 km s^{-1} is more likely to be in between the Scutum arm and Norma arms (Reid et al. 2016, 2019). Therefore, while the main component is likely at a distance of ∼2 kpc, the 30–50 km s^{-1} is in between 3 and 4 kpc. The emission in the range >50 km s^{-1} is more scattered and does not appear to correlate with the main bulk emission of M17. The ^{13}CO integrated intensity map in the velocity range 10–30 km s^{-1} also coincides with the submillimeter emission observed with ATLASGAL (see the three-color image of Figure 1). Subsequently, we considered only the emission around 10–30 km s^{-1}, as a part of M17, and used it to derive physical quantities.

4.2. Temperature and Column Density Distribution

Here we derive the excitation temperature, column density, and optical depth of the main cloud component of M17 (10–30 km s^{-1}) using our CO data (see also

Table 1
Gaussian Parameters Best Fitting the Averaged Spectra in Figure 4

Line	Component	Parameters	M17 Entire	M17-H II	M17-IRDC
	Gaussian 1	T [K]	10.9	9.1	10.5
		$V_{\rm LSR}$ [km s^{-1}]	20.3	20.0	20.1
		σ_v [km s^{-1}]	4.1	2.3	3.7
^{12}CO (J = 1–0)	Gaussian 2	T [K]	4.9	4.1	5.9
		$V_{\rm LSR}$ [km s^{-1}]	38.0	31.3	36.6
		σ_v [km s^{-1}]	6.9	11.7	7.4
	Gaussian 3	T [K]	1.9	1.8	2.1
		$V_{\rm LSR}$ [km s^{-1}]	57.0	57.0	59.3
		σ_v [km s^{-1}]	3.7	2.4	4.7
	Gaussian 1	T [K]	2.8	2.1	3.5
		$V_{\rm LSR}$ [km s^{-1}]	20.6	19.8	20.2
		σ_v [km s^{-1}]	3.0	2.0	2.4
^{13}CO (J = 1–0)	Gaussian 2	T [K]	0.8	0.8	0.9
		$V_{\rm LSR}$ [km s^{-1}]	36.7	30.5	34.1
		σ_v [km s^{-1}]	6.3	8.3	6.9
	Gaussian 3	T [K]	0.2	1.6	0.2
		$V_{\rm LSR}$ [km s^{-1}]	57.4	68.1	57.6
		σ_v [km s^{-1}]	2.6	1.8	2.8

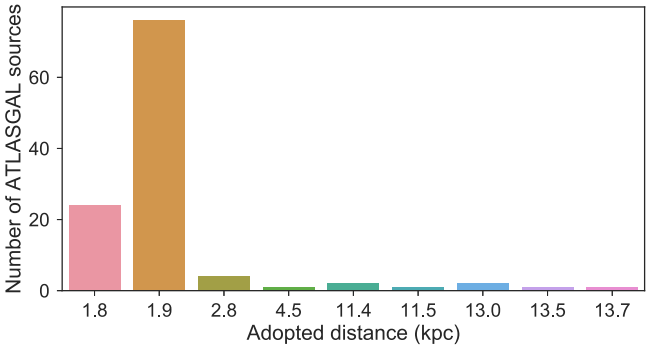

Figure 5. Histogram of distances of ATLASGAL sources extracted from Urquhart et al. (2018).

Mangum & Shirley 2015 for the derivation of these physical quantities). Based on the differences of ^{12}CO and ^{13}CO in the global integrated maps, we divide these cubes using different masked regions. Mask 1 is set to the region where both of the ^{12}CO and ^{13}CO integrated intensities are more than three times as high as the noise levels of 0.22 K km s^{-1} in the ^{12}CO integrated map and 0.089 K km s^{-1} in the ^{13}CO integrated maps. Mask 2 is set to the region where only the ^{12}CO emission is detected above 3σ = 0.27 K km s^{-1}. Mask 3 is set to the region where neither ^{12}CO nor ^{13}CO is detected above 3σ levels, which can be regarded as an emission-free region.

We assume that ^{12}CO and ^{13}CO have the same excitation temperature $T_{\rm ex}$, and that it can be calculated from the maximum main-beam brightness temperature of ^{12}CO, $T_{\rm max}(^{12}{\rm CO})$, in the masked region 1 as

$$T_{\rm ex} = \frac{5.5\ {\rm K}}{\ln\left(1 + 5.5\ {\rm K}/(T_{\rm max}(^{12}{\rm CO}) + 0.82\ {\rm K})\right)}. \quad (1)$$

The optical depth $\tau(^{13}{\rm CO})$ as a function of velocity in the masked region 1 can be derived from the main-beam brightness temperature $T_{\rm MB}(^{13}{\rm CO})$ as

$$\tau(^{13}{\rm CO})(v) = -\ln\left(1 - \frac{T_{\rm MB}(^{13}{\rm CO})}{f\,(J(T_{\rm ex}) - J(2.7\ {\rm K}))}\right). \quad (2)$$

Here the filling factor $f = 1$ is assumed as the extended nature of the emission and $J(T_{\rm ex}) = \frac{h\nu}{k\,(\exp(h\nu/kT_{\rm ex}) - 1)} = \frac{5.3}{(\exp(5.3/T_{\rm ex}) - 1)}$ for the ^{13}CO (J = 1–0) emission. h, k, and ν are Planck constant, Boltzmann constant, and transitional frequency. Subsequently, the ^{13}CO column density can be derived as

$$N(^{13}{\rm CO}) = \frac{3h}{8\pi^3 S\mu^2}\frac{Q_{\rm rot}}{g_{\rm u}}\frac{\exp(5.3/T_{\rm ex})}{\exp(5.3/T_{\rm ex} - 1)}\int \tau(v)dv, \quad (3)$$

where $\mu = 0.112$ D, $S = \frac{J_{\rm u}}{2J_{\rm u}+1}$ with $J_{\rm u} = 1$, and $g_{\rm u} = 2J_{\rm u} + 1 = 3$. The rotational partition function is approximated as $Q_{\rm rot} = \frac{kT_{\rm ex}}{hB} + \frac{1}{3}$ with B = 55101.011 MHz with the assumption that all the levels have the same $T_{\rm ex}$ and that $T_{\rm ex}$ is much higher than 5.3 K. This assumption might be wrong but is conventional, which is commonly called the LTE approximation. We convert the ^{13}CO column density to H_2 column density assuming a ^{13}CO fractional abundance of 2×10^{-6} (Dickman 1978). We use the updated conversion ratio $N_{\rm H_2}/N_{\rm CO} = 6000$ from Lacy et al. (2017), which yielded a ^{13}CO fractional abundance of 2.5×10^{-6} using the ratio ^{12}C/ ^{13}C = 60 specifically calculated for M17 (Henkel et al. 1982) and agreed with the average Galactic value (Langer & Penzias 1990).

For mask 2 region, we use the ^{12}CO (J = 1–0) emission as a proxy to estimate the H_2 column density assuming that the emission is optically thin as $N_{\rm H_2} = XW({\rm CO})$, where X is the conversion factor and W(CO) is the ^{12}CO (J = 1–0) integrated intensity. The X factor $X = 2 \times 10^{20}$ cm^{-2} K^{-1}(km s^{-1})$^{-1}$ is used as recommended by Bolatto et al. (2013), which was established after an exhaustive investigation of all possible

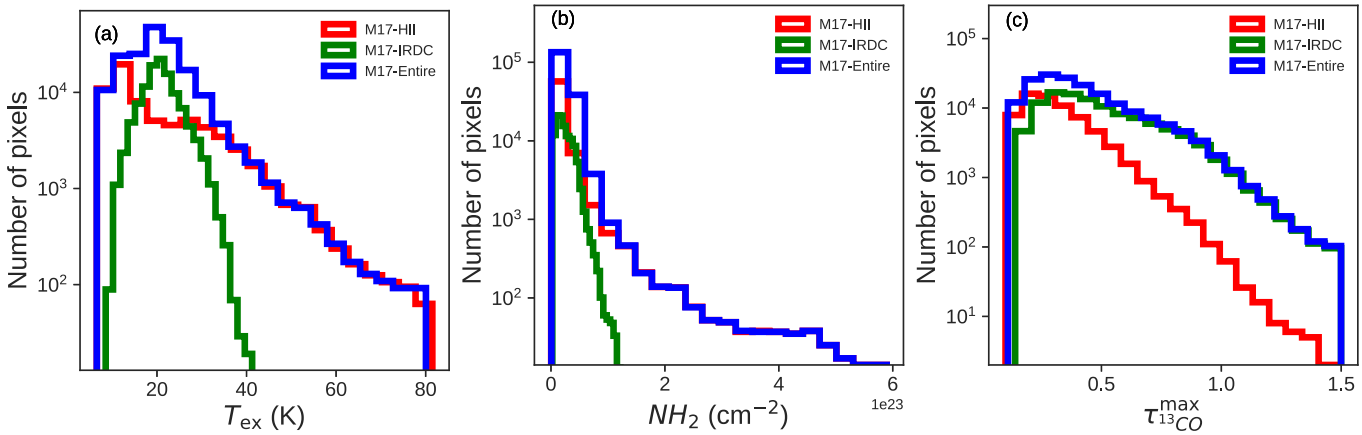

Figure 6. Histograms of the (a) CO excitation temperature, (b) H_2 column density, and (c) peak optical depth of the M17 region. The blue, orange, and green histograms are toward the entire M17, M17-H II, and M17-IRDC, respectively.

measurements. Note that we do not estimate T_{ex} for this masked region.

Excluding pixels where the excitation temperature is less than 2.7 K (14% number of pixels) due to low rms in the integrated maps, and using only non-zero data within the percentile range 0.5%–99.99%, we obtain a temperature range of 8–81 K, and an N_{H_2} range of 3×10^{20}–4.6×10^{23} cm^{-2} for the entire M17 complex (Figures 6 and 7). The median CO excitation temperature is ~20 K, and the median column density is 1.3×10^{22} cm^{-2} for the entire M17 (Table 2).

There are strong differences between M17-H II and M17-IRDC. First, the peak optical depth $\tau^{max}_{^{13}CO}$ is remarkably different in two regions, as seen in Figures 6 and 7. $\tau^{max}_{^{13}CO}$ in M17-H II has a mean value of 0.31 and a standard deviation of 0.15, while those of M17-IRDC are 0.5 and 0.24, respectively. Some regions in M17-IRDC have $\tau^{max}_{^{13}CO}$ values that are even higher than 1. Second, M17-H II has much higher temperatures than M17-IRDC. The maximum temperature in the M17-H II region reaches 81 K, especially around the NGC 6618 cluster, whereas the maximum temperature in M17-IRDC is only 41 K (Figure 7(a)). Third, in addition to being colder, M17-IRDC also has a lower peak column density compared to M17-H II (Figure 7(b)). We caution that the column density is probably overestimated because the partition function is overestimated due to the fact that T_{ex} is not much greater than 5.5 K.

4.3. Dense Gas Mass Function (DGMF) and Mass Properties

Figure 7(b) clearly shows that M17-H II has higher column density materials than M17-IRDC. The DGMF is useful to see how the dense gas is concentrated in specific density ranges. Dividing the column density into 120 column density bins ranging from 10^{21} cm^{-2} to 10^{24} cm^{-2} we create the DGFMs as the normalized cumulative mass distribution (CMD) as

$$\mathrm{DGMF}(>N_{H_2}) = \frac{\int_{N_{H_2}}^{N^{max}_{H_2}} \mu m_H A(N_{H_2}) dN_{H_2}}{M_{tot}}, \quad (4)$$

where N_{H_2} is the column density from which the mass is accumulated, $\mu = 2.8$ is the mean molecular weight, m_H is the hydrogen atomic mass, A is the integrated area, and $N^{max}_{H_2}$ is the maximum column density observed in the region. When N_{H_2} reaches the noise level $N^{min}_{H_2}$, the obtained mass is the total mass of the cloud M_{tot} in both masks 1 and 2. $N^{min}_{H_2}$ is the column density corresponding to the 3σ levels (Table 2). DGMFs for M17, M17-H II, and M17-IRDC are plotted in a log–log scale in Figure 8. They have flat profiles below the column density ~7×10^{21} cm^{-2} and then a quick drop to a power-law tail at higher column density. The column density ~7×10^{21} cm^{-2} is argued to be the threshold for star formation (André et al. 2010; Lada et al. 2010; Heiderman et al. 2010; Arzoumanian et al. 2011; Evans et al. 2014). The slope of the power-law tail is shallower in the M17-H II region than in the M17-IRDC region. DGMFs converge to unity toward lower column density, but diverge at higher column density. These profiles are similar to CMDs and DGMFs of other regions (Lada et al. 2010; Kainulainen et al. 2013, and Rivera-Ingraham et al. 2015).

We calculate the very dense gas mass fraction, the ratio of mass that has a column density higher than 1×10^{23} cm^{-2} or 1 g cm^{-2}, a column density level suggested as massive star formation threshold (Krumholz & McKee 2008) as

$$f_{verydense} = \frac{M_{N_{H2}>1\times10^{23}\ cm^{-2}}}{M_{tot}}. \quad (5)$$

In total, $f_{verydense}$ is about 8.86% in the entire M17. Individually, $f_{verydense}$ is 27% in M17-H II and only 0.46% in M17-IRDC region.

On the other hand, the DGMFs for mass with column density above the presumed threshold for star formation 7×10^{21} cm^{-2} are 96%, 91%, and 98.5% for M17, M17-H II, and M17-IRDC, respectively. These two column density levels are marked as vertical lines in Figure 8.

The flat plateau of the DGMF at the low column density part gives us the total masses of M17, M17-H II, and M17-IRDC (Figure 8), which are captured in Table 2. The total mass of M17 is 4.49×10^5 $M_\odot$, that of M17-H II is 1.43×10^5 $M_\odot$, and that of M17-IRDC is 3.06×10^5 $M_\odot$. The median pixel-by-pixel mass surface density of M17-IRDC (614 $M_\odot$ pc^{-2}) is higher than that of the M17-H II region (280 $M_\odot$ pc^{-2}). However, the peak mass surface density is much higher in M17-H II (9831 $M_\odot$ pc^{-2}) than in M17-IRDC (1995 $M_\odot$ pc^{-2}) (see Table 2). The mean column density $N^{mean}_{H_2}$ is calculated as

$$N^{mean}_{H_2} = \frac{M_{tot}}{A_{tot}}, \quad (6)$$

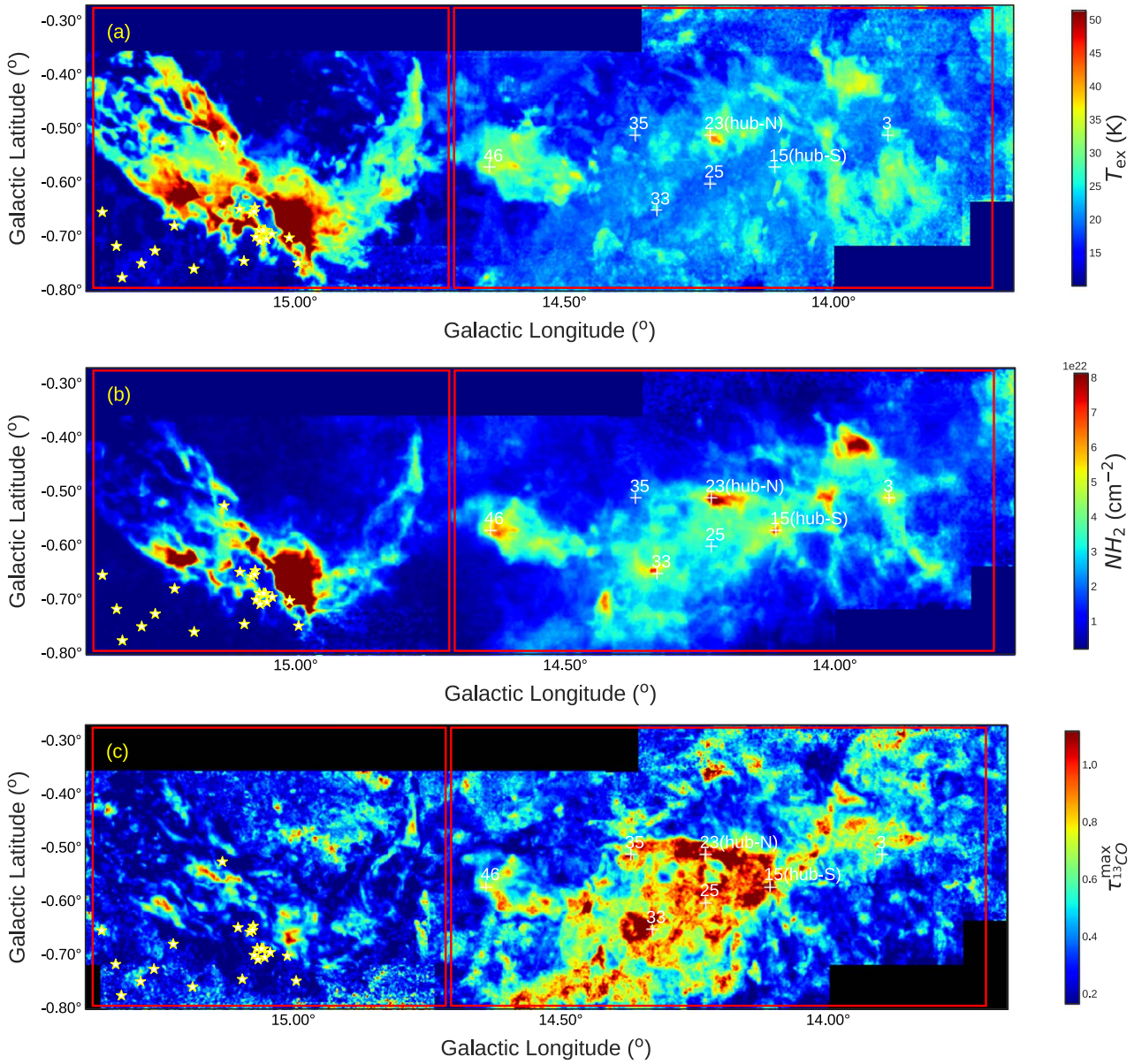

Figure 7. Maps of the (a) CO excitation temperature, (b) H_2 column density, and (c) peak optical depth of the M17 complex. We use only data within the main velocity range (10–30 km s^{-1}) of M17. The red rectangles outline the two prominent star-forming regions: M17-H II (left) and M17-IRDC (right). The star symbol pinpoints the OB star cluster responsible for the giant H II region. The cross symbols pinpoint the locations of the massive cores ($M > 500\,M_\odot$) reported by Shimoikura et al. (2019a).

Table 2
Properties of the Subregions M17-H II, M17-IRDC, and the M17 Complex

Region	$(T_{ex}^{min}, T_{ex}^{median}, T_{ex}^{max})$ (K)	$(N_{H_2}^{min}, N_{H_2}^{median}, N_{H_2}^{max})$ (10^{21} cm^{-2})	$(\Sigma_{gas}^{min}, \Sigma_{gas}^{median}, \Sigma_{gas}^{max})$ ($M_\odot$ pc^{-2})	A_{tot} (pc^2)	M_{tot} ($M_\odot$)	$n_{H_2}^{mean}$ (cm^{-3})
M17-H II	(8, 15, 81)	(0.3, 6.3, 458)	(6, 134, 9831)	364	1.43×10^5	166
M17-IRDC	(11, 21, 41)	(1.9, 17, 93)	(40, 355, 1995)	593	3.06×10^5	285
M17	(8, 20, 81)	(0.3, 13, 458)	(6, 281, 9831)	957	4.49×10^5	201

Note. T_{ex}, N_{H_2}, and Σ_{gas} are measured per pixel.

where A_{tot} is the total areas of the clouds calculated as the sum of areas of all interior pixels of the cloud projection on the plane of the sky. We also calculate the volume density as $n_{H_2} = \frac{M}{V} = \frac{M}{\frac{4}{3}\pi r^3}$ where $r = \sqrt{\frac{A_{tot}}{\pi}}$ and A_{tot} is tabulated in Table 2. The mean volume density is higher in M17-IRDC (285 cm^{-3}) than in M17-H II (166 cm^{-3}). For the two column density levels discussed above, the corresponding average volume densities of M17-H II, M17-IRDC, and entire M17,

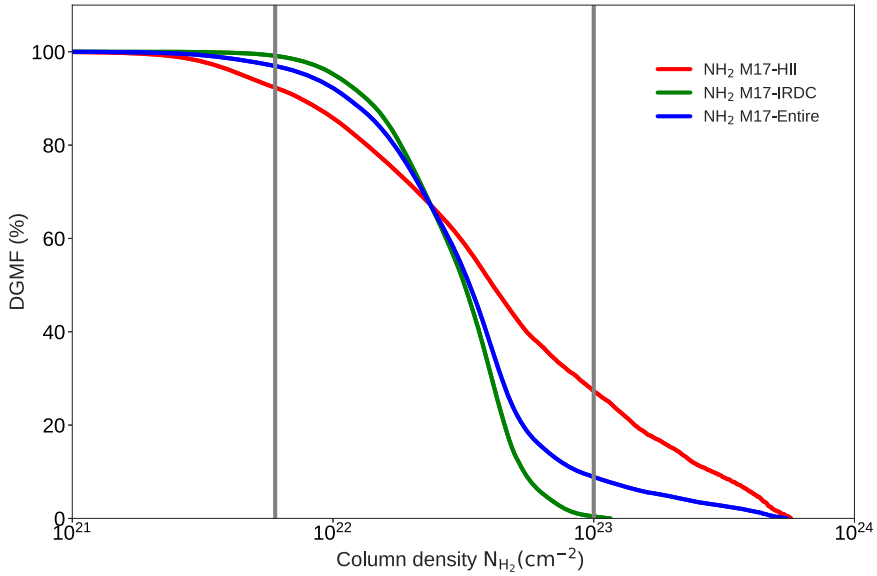

Figure 8. Normalized cumulative column density distributions of the entire M17, M17-H II, and M17-IRDC regions. The vertical lines mark the locations of the column densities of 7×10 and 1×10^{23} cm^{-2}.

Table 3
Statistics of Individual Clumps Extracted with the Dendrogram Technique in the M17-H II, M17-IRDC, and the Entire M17 Clouds

Region	$n_{\rm sources}$	$n_{\rm sources}(\alpha_{\rm vir} > 1)$	($R^{\rm min}$, $R^{\rm median}$, $R^{\rm max}$) pc	($M^{\rm min}$, $M^{\rm median}$, $M^{\rm max}$) $M_\odot$	($\alpha_{\rm vir}^{\rm min}$, $\alpha_{\rm vir}^{\rm median}$, $\alpha_{\rm vir}^{\rm max}$)
M17-H II	26	11	(0.12, 0.2, 0.41)	(3, 60, 1719)	(0.12, 0.86, 8.23)
M17-IRDC	164	105	(0.11, 0.2, 0.54)	(1, 14, 1001)	(0.14, 1.36, 14.23)
M17-Entire	190	116	(0.11, 0.2, 0.54)	(1, 17, 1719)	(0.12, 1.33, 14.23)

respectively, are 1.0×10^5, 2.1×10^5, and 9.5×10^4 cm^{-3} for column density above 1×10^{23} cm^{-2}, and 3.5×10^3, 1.7×10^3, 1.5×10^3 cm^{-3} for column density above 7×10^{21} cm^{-2}.

In summary, the peak column density is higher in M17-H II while the average column density and total mass are higher in M17-IRDC. If very dense gas is considered alone, its average volume density is approximately two times more in M17-H II than in M17-IRDC.

4.4. Individual Clump Structure Extracted with Dendrogram

To obtain an automatic extraction of the individual clumps in M17, we use the Dendrogram (Rosolowsky et al. 2008).[14] It is a hierarchical clustering method that builds up clusters in a tree-like structure where each node represents a leaf (structure that has no sub-structure) or branch (structure that has successor structure). Each node in the cluster tree contains a group of similar data. Clusters at one level join with clusters in the next level up using a degree of similarity. The total number of clusters is not predetermined.

In our extraction, we use Dendrogram to detect and extract the morphologies of individual clumps using the ^{12}CO ($J = 1$–0) data cube in the velocity range of 10.0–30.0 km s^{-1}. We extract only sources in the regions that have a column density above 3×10^{22} cm^{-2}, as in the masked map (Figure 17). This threshold corresponds to three times the median column density of the entire map (Table 2). Dendrogram requires three input parameters: `min_value`, `min_delta`, and `min_npix`. The first parameter `min_value` specifies the minimum value above which Dendrogram attempts to identify the structures. The second parameter `min_delta` is the minimum step required for a structure that has been identified. The third parameter `min_npix` is the minimum number of pixels that a structure should contain in order to remain an independent structure. We set the three parameters as follows: `min_value` $= 5\sigma$, `min_delta` $= 3\sigma$, and `min_npix` $= 100$, where σ is the average rms noise level of the ^{12}CO data. We select `min_npix` $= 100$ which is in the middle of $4 \times 4 \times 4 = 64$ and $5 \times 5 \times 5 = 125$ voxels in position–position–velocity space in order to remove artificial structure in the area having high noise after some trials. The map angular resolution is close to about four times the cell size. We keep only leaf structures, which are independent structures in our analysis. This extraction with Dendrogram results in the identification of 26 individual clumps in the M17-H II and 164 clumps in M17-IRDC. The properties of these clumps can be found in Table 3. Here, we assumed all the distances to the structures identified are equal to the representative distance of $d = 2$ kpc.

We use the virial parameters as the ratio of the virial mass to the true clump mass, "$\alpha_{\rm vir}$," as a measure of the gravitational stability of the clumps. For clumps in gravitational equilibrium, $\alpha_{\rm vir}$ is unity. Collapsing and dispersing clumps have $\alpha_{\rm vir}$ of <1 and >1, respectively. The virial parameter for a spherical

[14] https://Dendrograms.readthedocs.io/en/stable/

clump with uniform density and temperature neglecting external pressure and magnetic field can be expressed as

$$\alpha_{\rm vir} = \frac{M_{\rm vir}}{M_{\rm clump}} = \frac{5\sigma_{\rm 3D}^2 R}{3GM_{\rm clump}}, \quad (7)$$

where G, M, and R are the gravitational constant, clump mass and clump radius, respectively (Bertoldi & McKee 1992). The clump radius R is defined as the geometric mean of the major and minor semi-axes of the projection onto the position–position plane for a clump identified. 3D velocity dispersion $\sigma_{\rm 3D}$ is calculated as $\sigma_{\rm 3D} = \sigma_{\rm 1D}/\sqrt{3}$. The clump mass is the LTE mass calculated from the ^{12}CO (J = 1–0) integrated intensity of the individual structures.

The masses of the individual clumps extracted with Dendrogram in M17-H II appear to be comparable to those in M17-IRDC, while the peak column density in M17-H II is higher than that in M17-IRDC, as seen in the histogram of column density (Figure 8). The median clump mass is 60 and 14 $M_\odot$ in M17-H II and M17-IRDC, respectively. Both clumps in M17-H II and M17-IRDC have a median radius of 0.2 pc. The virial parameters of clumps in M17-H II are smaller than those in M17-IRDC. We find that 64% of clumps in M17-IRDC have virial parameters $\alpha_{\rm vir} > 1$, while 42% of clumps in M17-H II have $\alpha_{\rm vir} > 1$. However, the median virial parameter in M17-IRDC is 1.36, higher than the median value of 0.86 in M17-H II. Thus, the clumps in M17-H II are more prone to gravitational contraction, which is consistent with the fact that star formation is much more active in M17-H II.

4.5. Distribution of Dense Gas Traced by HCO^+ and HCN

M17-H II and M17-IRDC have different high column density gas concentration in the column density maps created from CO (J = 1–0) observations, as discussed in Section 4.2. We use HCO^+ (J = 1–0) and HCN (J = 1–0) to further examine the distribution of high-density gas in M17, which are thought to be better tracers of dense star-forming gas than CO isotopologues (Gao & Solomon 2004; Wu et al. 2010; Stephens et al. 2016). The optically thin critical densities of HCO^+ (J = 1–0) are as high as 6.8×10^4 cm^{-3} and that of HCN (J = 1–0) is as high as 4.7×10^5 cm^{-3} at 10 K (Shirley 2015). However, the effective critical densities at the same temperatures are 9.5×10^2 cm^{-3} for HCO^+ (J = 1–0) and 8.4×10^3 cm^{-3} for HCN^+ (J = 1–0). For comparison, the critical density of ^{12}CO (J = 1–0) is less than 10^3 cm^{-3} (Shirley 2015). Besides tracing the general landscape of dense gas, these tracers are sensitive to the physical processes closely related to star formation, such as outflows, infall, photoionization, mechanical energy, and chemistry (Fuller et al. 2005; Roberts et al. 2011; Sanhueza et al. 2012; Chira et al. 2014; Walker-Smith et al. 2014; Shimajiri et al. 2017).

In Figure 9, we present the integrated intensity maps of HCN and HCO^+ (J = 1–0) transitions from 10 to 30 km s^{-1}. The 1σ levels are ~1 and 1.2 K km s^{-1} for the HCN and HCO^+ integrated maps. It clearly shows that most of the emission of these lines is in the M17-H II region, indicating that the M17-H II region contains a significant amount of high-density gas. The HCO^+ and HCN emission come mainly from the high column density (>3×10^{22} cm^{-2} or 600 $M_\odot$ pc^{-2}) part traced in CO, except near the star cluster where the column density is lower than 3×10^{22} cm^{-2} but a small fraction of HCO^+ and HCN (J = 1–0) is still detected. In contrast, the emission of HCO^+ and HCN in M17-IRDC is almost invisible, except in a few dense clumps and intersections of the IRDC filamentary network (Busquet et al. 2016), indicating that there is more dense gas at the intersections of the filaments (Ohashi et al. 2016). These locations coincide with the bright ^{13}CO emission positions (see Figure 19). Note that these areas of both HCN and HCO^+ emission are similar and are the sums of all pixels that have HCN and HCO^+ emission larger than zero. The total areas of HCN/HCO^+ of H II and M17-IRDC are 23.6 pc^2 and 52.6 pc^2, respectively. Thus, the HCN and HCO^+ emitting areas are 6.5% and 8.9% of the total CO emitting areas for H II and M17-IRDC, respectively. While the trends are similar, HCN integrated intensity is higher than that of HCO^+. The maximum HCO^+ integrated intensity in M17-IRDC is about 5 K km s^{-1}, while that of M17-H II goes up to 35 K km s^{-1}.

While the integrated intensities of HCN and HCO^+ depend linearly on the gas column density in the M17-H II cloud (Figure 10(a)), they do not exhibit similar correlation in M17-IRDC (Figure 10(b)). The Spearman correlation coefficients of HCN and HCO^+ versus gas column density are 0.72 and 0.68 in M17-H II cloud, and they are both 0.54 in M17-IRDC. A similar trend is also found between the integrated intensities of HCN and HCO $^+$ and excitation temperature, except the linear dependence of the integrated intensities of HCN and HCO^+ only appears at temperature higher than 50 K (Figures 11(a) and 11(b)). The Spearman correlation coefficients of HCN and HCO^+ versus excitation temperature are lower: 0.65 and 0.59 in M17-H II cloud, and they are 0.49 and 0.39 in M17-IRDC, respectively. The mean ratios of HCO^+/HCN are ~0.73 in M17-H II and ~0.97 in M17-IRDC. While the mean ratio in M17-H II is similar to values obtained for resolved nearby galaxies in a recent survey (Jiménez-Donaire et al. 2019), that of M17-IRDC is higher. Compared to Galactic Cloud, the ratio of of HCO^+/HCN in M17-H II is comparable to Ophiuchus (0.77) and higher than Aquila (0.63) but lower than Orion B (from 0.9 to 1.4), while the value of M17-IRDC is more comparable to those of Orion B (Shimajiri et al. 2017).

5. Discussion

In the previous Section, we have quantified the difference between M17-H II and M17-IRDC in terms of the cloud mass distribution and the distribution of dense gas tracers. In this Section, we will discuss the difference between two subregions and how their distributions impact star formation in M17.

5.1. Two Distinct Subregions in the M17 Cloud Complex

M17-H II and M17-IRDC clouds have different physical properties, as shown in Section 4 and are also known for having different star formation activity (Povich & Whitney 2010; Povich et al. 2016). We summarize the properties of the two subregions in Figure 12. M17-H II is harboring a massive protostellar cluster (Kuhn et al. 2015), while M17-IRDC is quiescent and currently forming low-mass stars (Ohashi et al. 2016). M17-H II is warmer and has higher peak column density and a much higher very dense gas fraction. M17-IRDC is more massive and has a higher mean surface density. The total fraction of $\frac{L_{\rm HCN\,J=1-0}}{L_{\rm HCO^+\,J=1-0}}$ and fraction of dense gas area over CO gas area are also higher in M17-H II (see Section 5.2).

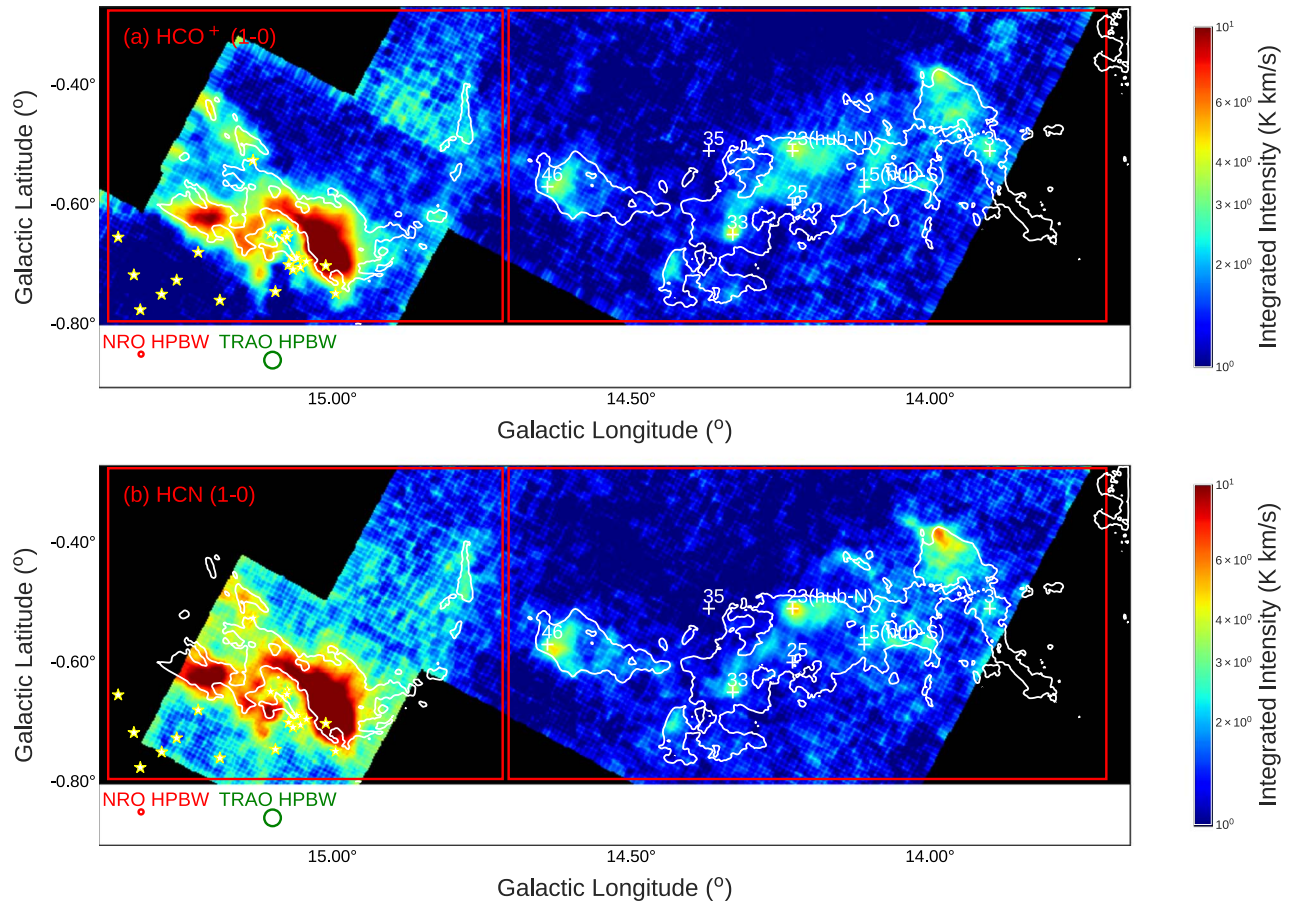

Figure 9. (a) The HCO^+ ($J = 1$–0) and (b) HCN ($J = 1$–0) integrated intensity maps of M17. The red rectangles outline the two prominent star-forming regions: M17-H II (left) and M17-IRDC (right). The star symbols pinpoint the OB star clusters responsible for the giant H II region. The cross symbols pinpoint the locations of the massive cores ($M > 500\ M_\odot$) reported by Shimoikura et al. (2019a). The white contours correspond to the gas column density level of 3×10^{22} cm^{-2}.

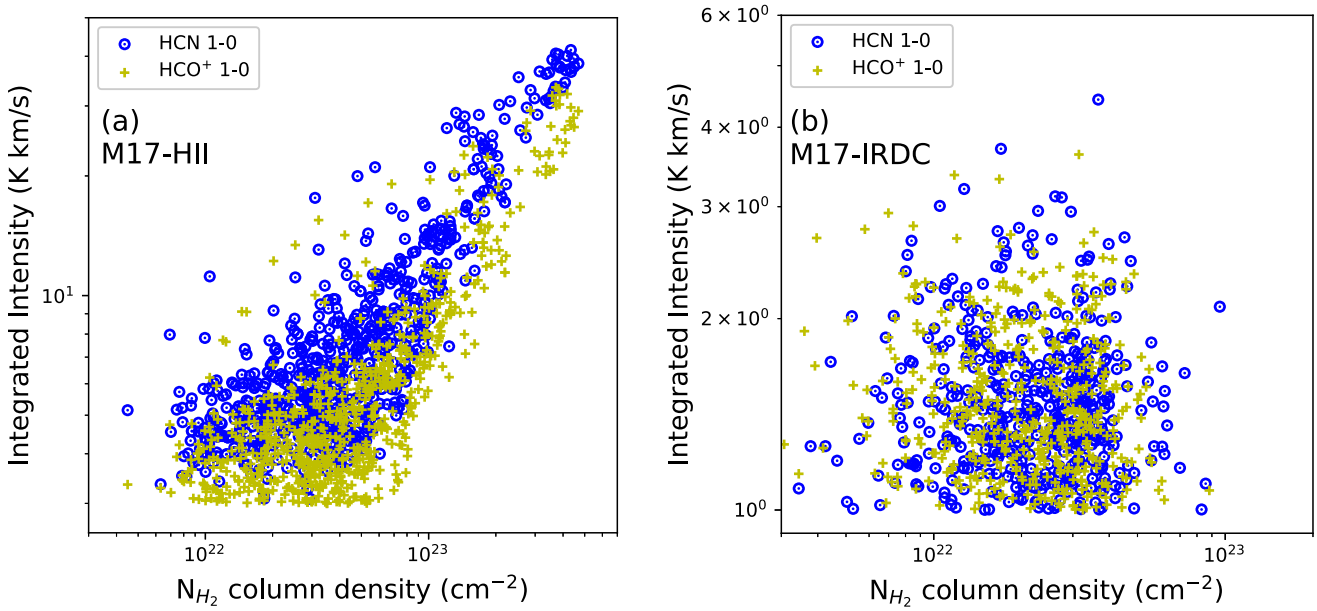

Figure 10. Scatter plots of pixel-by-pixel HCN and HCO^+ ($J = 1$–0) integrated intensity vs. gas column density for (a) M17-H II and (b) M17-IRDC regions. We note that the scales are different in these plots.

5.2. HCO^+ and HCN ($J = 1$–0) as Proxies to Trace Dense Gas Mass

The distributions of HCO^+ and HCN ($J = 1$–0) coincide with the high-density part of the gas column density map, suggesting that HCO^+ and HCN ($J = 1$–0) emission lines trace a similar density region (Figures 9(a) and 9(b)). As in Section 4.3, we divide the integrated intensity maps of HCN and HCO^+ ($J = 1$–0) into 120 bins based on the gas column

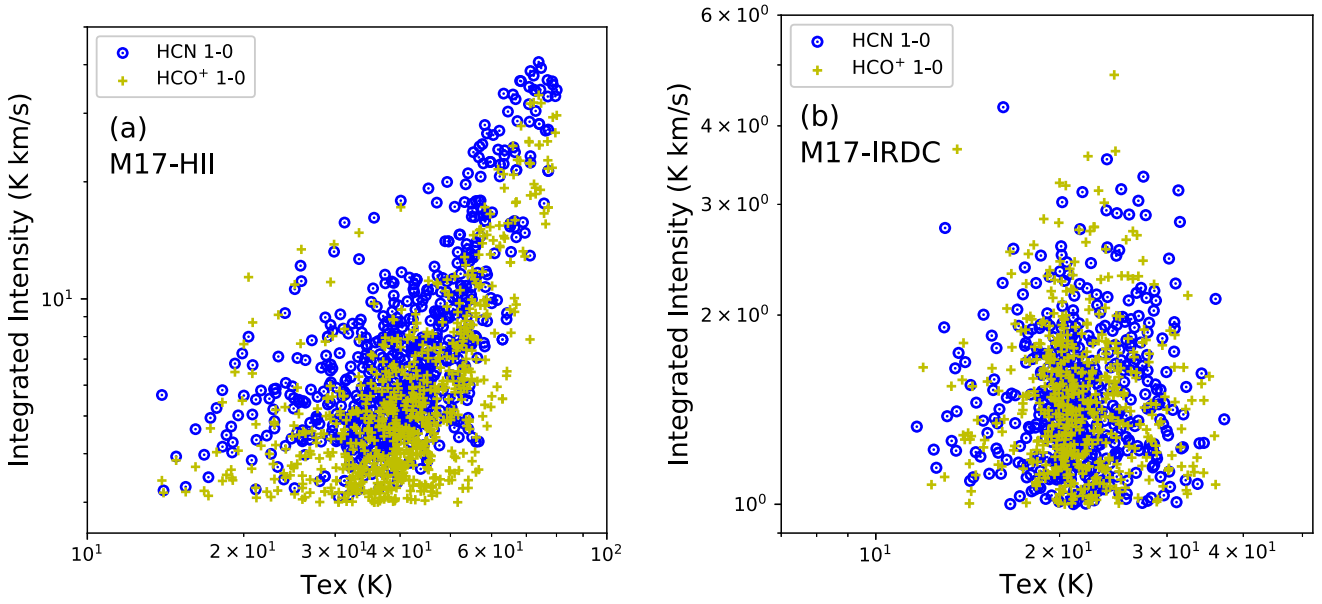

Figure 11. Scatter plots of pixel-by-pixel HCN and HCO^+ ($J = 1$–0) integrated intensity vs. gas temperature for (a) M17-H II and (b) M17-IRDC regions. We note that the scales are different in these plots.

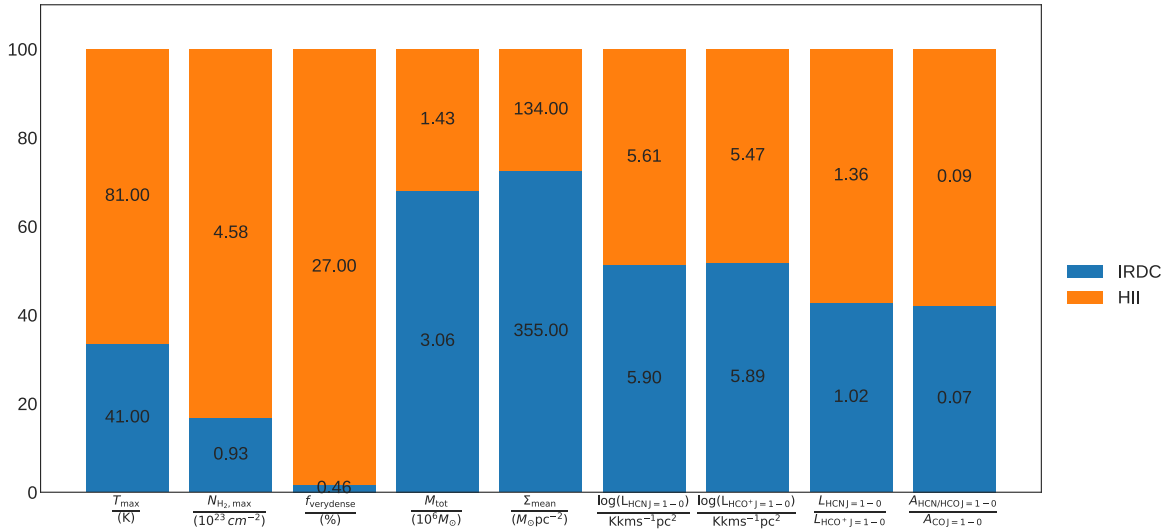

Figure 12. Comparison of different physical properties of the M17-H II and M17-IRDC clouds: maximum excitation temperature $T_{\rm max}$, maximum column density $N_{\rm H_2,max}$, very dense gas ($N_{\rm H_2} > 1 \times 10^{23}$ cm^{-2}) ratio $f_{\rm verydense}$, total mass $M_{\rm tot}$, mean gas surface density $\Sigma_{\rm mean}$, HCN $J = 1$–0 line luminosity, HCO^+ $J = 1$–0 line luminosity, HCN $J = 1$–0/HCO^+ $J = 1$–0 line-luminosity ratio, ratio of dense gas area over total gas area $A_{\rm HCNorHCO^+}/A_{\rm CO}$.

density bins ranging from 10^{21} cm^{-2} to 10^{24} cm^{-2}. We then calculate the line-luminosity function (LLF) in the formed of the normalized cumulative line-luminosity function (nCLLF) as

$$\mathrm{LLF}(>N_{\rm H_2}) = \frac{\int_{N_{\rm H_2}}^{N_{\rm H_2,max}} A(N_{\rm H_2}) dL_{\rm line}(N_{\rm H_2})}{\int_{0}^{N_{\rm H_2,max}} A(N_{\rm H_2}) dL_{\rm line}(N_{\rm H_2})}. \quad (8)$$

We use the same approach detailed in Solomon et al. (1997) or Wu et al. (2010) to calculate the line luminosity as

$$L_{\rm line} = 23.5 \Omega_{s*b} D_{\rm L}^2 I_{\rm line} (1+z)^{-3}, \quad (9)$$

where Ω_{s*b} is the source solid angle convolved with the telescope beam and has a unit of arcsec^2. $D_{\rm L}$ is the luminosity distance and is in units of Mpc, $I_{\rm line}$ is the integrated line intensity and is in units of K km s^{-1}. z is the redshift of the object. The luminosity is expressed in units of K km s^{-1} pc^2. If the source is much smaller than the beam, then Ω_{s*b} is equal to the beam size Ω_b. In the case of Galactic clumps and clouds, the sources are often more extended than the beam, and the source solid angle convolved with a Gaussian beam is expressed as

$$\Omega_{s*b} = \left(\frac{\pi \times \theta_s^2}{4ln2}\right)\left(\frac{\theta_s^2 + \theta_{\rm beam}^2}{\theta_s^2}\right). \quad (10)$$

Therefore, the line luminosity in units of K km s^{-1} pc^2 of an object in the Milky Way ($z = 0$) can be derived as

$$L_{\rm line} = 23.5 \times 10^{-6} \Omega_{s*b} d^2 I_{\rm line}, \quad (11)$$

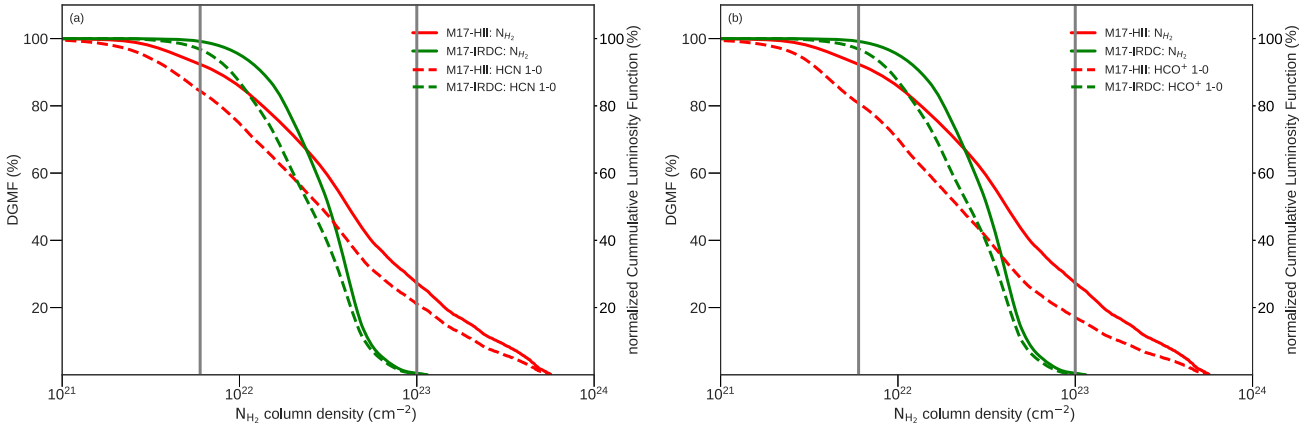

Figure 13. HCN (a) and HCO^+ ($J = 1$–0) (b) normalized cumulative luminosity compared to the gas column density CMD.

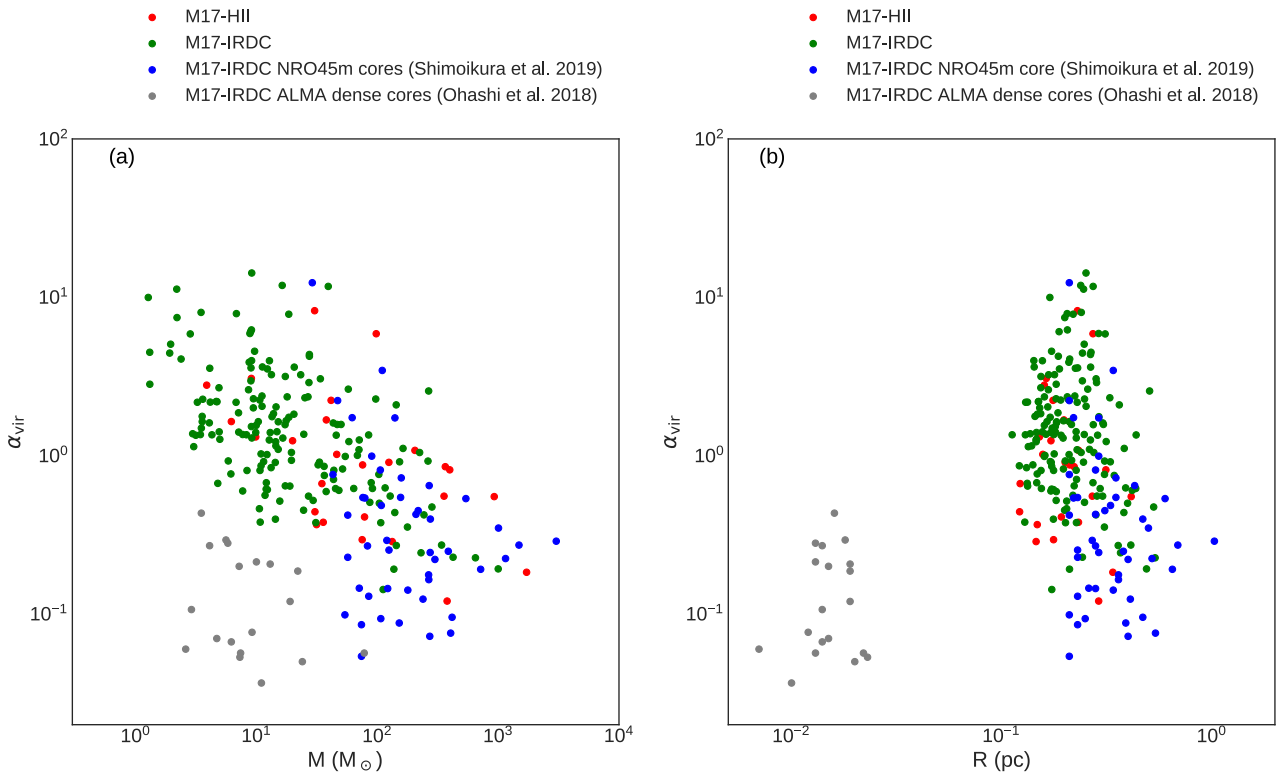

Figure 14. Virial parameters as functions of (a) mass and (b) radius of individual clumps in the M17-H II (red) and M17-IRDC regions (green). Virial parameters of N_2H^+ ($J = 1$–0) cores (blue) derived from NRO 45 m observations (Shimoikura et al. 2019a) and N_2H^+ ($J = 1$–0) dense cores (gray) derived from ALMA observations (Ohashi et al. 2016) are also plotted.

where d is distance and has units of kpc and T_{MB} is the main-beam brightness temperature of the line. The line luminosity can be converted from K km s^{-1} pc^2 to solar bolometric luminosity units as in Nguyen-Luong et al. (2013). The line-luminosity functionN_{H_2} profiles are shown in Figure 13, where they are also compared with DGMFs.

The luminosity functions of both lines span the entire column density range traced by the gas column density and are shallower than the DGMF profiles. Therefore, both HCO^+ and HCN ($J = 1$–0) integrated intensities can serve as proxies for high column density dense gas tracers, at least at scales smaller than cloud scale. In contrast, other works have shown that HCN can trace more diffuse gas than HCO^+ (i.e., Kauffmann et al. 2017; Pety et al. 2017; Shimajiri et al. 2017). The difference comes from the fact that M17 is a massive star-forming regions, while the molecular clouds in other studies are low-mass forming regions.

While the luminosity functions of HCO^+ and HCN are similar in M17-IRDC, the HCN luminosity function is higher than that of HCO^+ in M17-H II. Therefore, the ratio of HCN/HCO^+ in M17-IRDC is lower than the ratio in M17-H II. Lower HCN/HCO^+ might be related to the quiescent state of the ongoing IRDC, while the higher ratio of HCN/HCO^+ might reflect the cloud at a more advanced states as free electrons in the turbulent and far-UV irradiated environment near the massive cluster can easily be recombined with HCO^+ (Papadopoulos 2007). This agrees with the fact that HCN is enhanced in an X-ray-dominated environment that is produced

by young massive stars in M17-H II. Actually, Meijerink & Spaans (2005) and Meijerink et al. (2007) show that a lower ratio is observed on the surface of the X-ray-dominated or photon-dominated region and a higher ratio is often seen in high-density and cold regions. Therefore, a high HCN/HCO^+ ratio might be a good indicator of massive star formation or more evolved evolutionary stages of star formation (see also Wu et al. 2010; Sanhueza et al. 2012).

5.3. Stability of Clumps in M17-IRDC and M17-H II

There are more unbound clumps in the M17-IRDC region than in the M17-H II region, as seen in the $\alpha_{\rm vir}$–M and $\alpha_{\rm vir}$–R relations in a log scale (Figure 14). We find that 64% of the clumps in M17-IRDC have $\alpha_{\rm vir} > 1$. In addition, the clumps in M17-IRDC have systematically higher virial parameters than those in M17-H II. These facts support the idea that the clumps in M17-H II are more prone to gravitational contraction, while those in M17-IRDC that have $\alpha_{vir} > 1$ are gravitationally unbound and dispersing. However, there is a chance that they can be in the gravitational equilibrium if surrounded by high external pressure (see Shimoikura et al. 2019a).

We compare the virial parameters of clumps in our studies with those of N_2H^+ ($J = 1$–0) cores (radius ~0.1–1 pc) obtained from observation also with NRO 45 m (Shimoikura et al. 2019a) and N_2H^+ ($J = 1$–0) dense cores (radius ~0.007–0.03 pc) obtained from observation with the ALMA interferometer (Ohashi et al. 2016). For the first data set, we derive the 3D virial parameter using their virial masses and core masses by applying Equation (7). For the second one, because their virial parameters are calculated as $\frac{5\sigma^2 R}{GM}$, we divide it by 3 to obtain the 3D virial parameters. While all ALMA dense cores have $\alpha_{\rm vir} < 1$, most NRO 45 m cores have $\alpha_{\rm vir} < 1$ and some cores have $\alpha_{\rm vir} > 1$. The trend is consistent with the general suggestion that virial parameter increases with size (Ohashi et al. 2016; Chen et al. 2019). We suggest that virial parameter increase with size until the core size reaches ~0.5–1 pc and decreases with size starting at the clump scales. We note that the 3D virial parameters of the molecular cloud complex (radius ~50–100 pc) are in the range of 0.5–3 (Nguyen-Luong et al. 2016).

We also examine the significance of external pressures by plotting the relationship between $\sigma^2_{\rm 3D}/R$ and the mass surface density $\Sigma_{\rm gas}$ in Figure 15, as theoretically suggested by Field et al. (2011) as

$$\frac{\sigma^2_{\rm 3D}}{R} = \frac{1}{3}\left(\pi\Gamma G\Sigma + \frac{4P_{\rm e}}{\Sigma}\right), \quad (12)$$

where Γ is a form factor that equals 0.73 for an isothermal sphere of critical mass with a centrally concentration internal density structure (Elmegreen 1989). $P_{\rm e}$ is the external pressure and is often expressed as $\frac{P_{\rm e}}{k}$ in units of K cm^{-3}.

When $P_{\rm e}$ equals 0, the cloud is in simple virial equilibrium (SVE), with the internal kinetic energy being equal to half the gravitational energy (Field et al. 2011). In Figure 15, we overlaid the SVE, line in addition to some curves with external pressure ranging from 10^3 to 10^7 K cm^{-3}. Contrary to the clumps in Heyer et al. (2009) that mostly lie above the SVE line, our data show that half of the clouds are above and half are below the SVE line. The first half is dynamically unstable due to external pressure, while the second half is gravitationally bound and collapses on its own gravity. This is an interesting

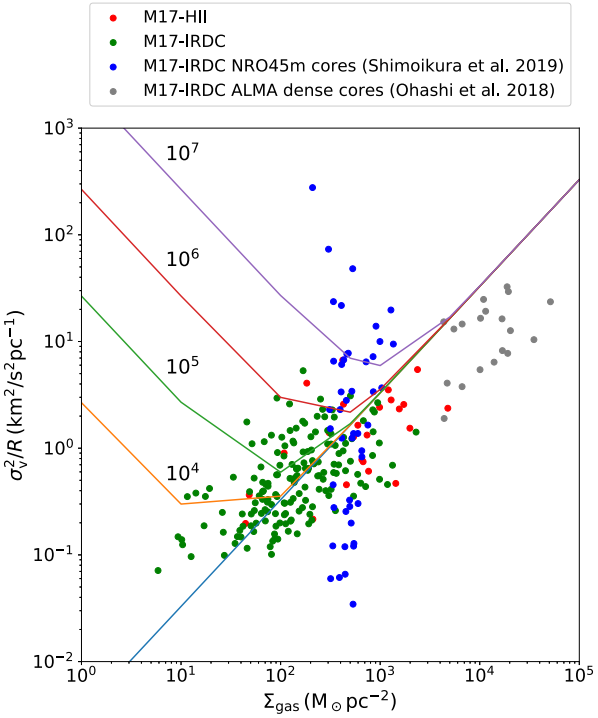

Figure 15. The line width–size scaling coefficient and mass surface density relation. The blue straight line shows the case where there is no external pressure. The orange, green, red, and pink curves show the cases where external pressure $P_{\rm e}/k$ is 10^4, 10^5, 10^6, and 10^7 K cm^{-3}, respectively.

fact since most of the high-resolution and high-density cores (Ohashi et al. 2016; Shimoikura et al. 2019a) can collapse on their, own while our CO clumps need external pressure to collapse. Another interesting fact is that most clumps in M17-IRDC live above the SVE line, which means they need additional external pressure to collapse while those in M17-H II do not. This fact is consistent with the higher virial parameters in M17-IRDC clumps and also consistent with what is found in molecular clouds in the Galactic Center (Miura et al. 2018).

5.4. Conditions for Massive Star Formation in M17 H II and M17-IRDC

The mass functions of YSOs in the M17-H II and M17-IRDC regions were derived by Povich & Whitney (2010) and Povich et al. (2016) using *Spitzer* data. They found that the high-mass stellar population is deficient in M17-IRDC, making it possible that the massive star formation is delayed in the M17-IRDC region assuming that the final stellar IMF approaches the Salpeter IMF. Here, we attempt to elucidate whether the present physical conditions of M17 satisfy the criteria of massive star formation, based on our observational results.

Krumholz & McKee (2008) proposed the threshold column density as one condition for massive star formation of $\Sigma > 1$ g cm^{-2} or $N_{H_2} > 10^{23}$ cm^{-2}, beyond which molecular clouds could form high-mass stars, avoiding further fragmentation to form lower-mass cores. As shown in Section 4, the cumulative column density distributions derived from our CO data (see Figure 8) clearly indicate that the M17-H II region is denser than the M17-IRDC region. In addition, the M17-H II region is more evolved in terms of forming stars and the M17-IRDC region is more quiescent. Although the median column density and total mass of M17-IRDC are larger than those of the M17-H II region, most of the clumps identified in M17-IRDC have

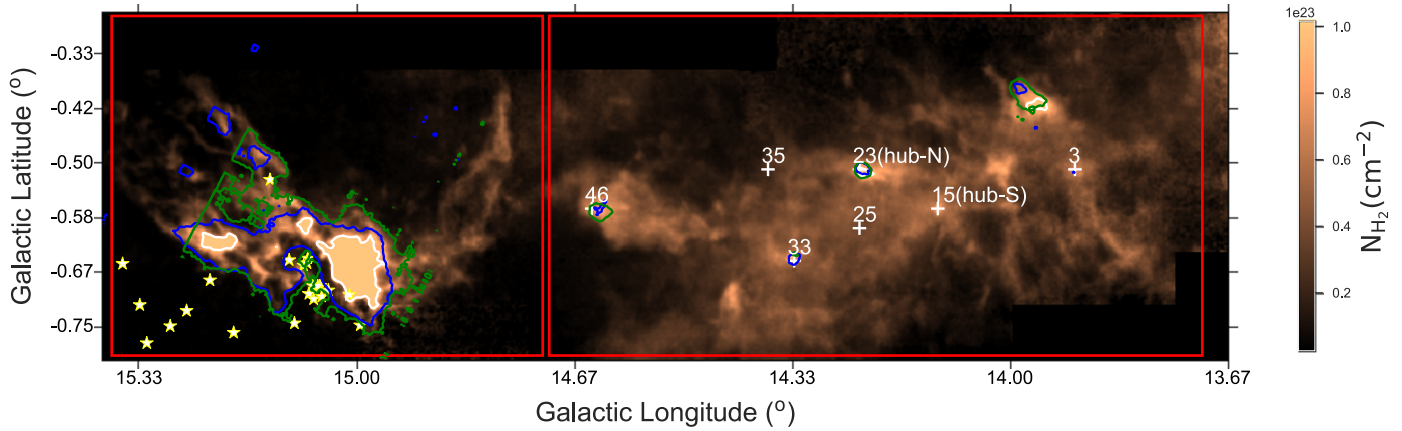

Figure 16. Gas column density maps and dense gas distribution. The colored scale image indicates the column density distribution derived from ^{13}CO. The white contour is at the column density of ∼1 g cm^{-2}. The blue contours represent the HCO$^+$ integrated intensity and the green contours represent the HCN integrated intensity, both at the 3.5 K km s^{-1} level. The star symbols pinpoint the OB star clusters responsible for the giant H II region. The cross symbols pinpoint the locations of the massive cores ($M > 500\ M_\odot$) reported by Shimoikura et al. (2019a).

column densities lower than the threshold of massive star formation. In contrast, M17-H II contains several clumps with column densities comparable to or larger than the threshold. For comparison, we show the dense region in M17 traced by HCO$^+$ and HCN $J = (1–0)$ emission in Figure 16. Therefore, we conclude that the current mass concentration in M17-IRDC is not enough to efficiently create high-mass stars. However, there is a large mass reservoir and a filamentary network that can feed the clumps and cores to grow up and later form high-mass stars (Ohashi et al. 2016). External pressure might be needed for the clumps in M17-IRDC to collapse and form stars as shown in Section 5.3.

5.5. What Could Be the Star Formation Scenario for the Entire M17 Cloud Complex?

In Section 4, we showed that the dense gas fraction and the dynamical states of the M17-H II cloud and clumps within it are different from those of M17-IRDC. Yet, both regions were suggested to be connected (Shimoikura et al. 2019a) and are formed by colliding clouds (M17-H II: Nishimura et al. 2018; M17-IRDC: Sugitani et al. 2019). In addition, Sugitani et al. (2019) used the the near-infrared polarization and CO ($J = 3–2$) data to discover that the main elongation axis of M17-IRDC is perpendicular to the global magnetic fields, which are roughly perpendicular to the Galactic plane. Such a structural and magnetic configuration might be consistent with molecular cloud formation by the Parker instability (Parker 1966; Shibata et al. 1992). Since Parker instability is more unstable to the anti-symmetric mode, the field lines tend to cross the Galactic plane. According to the linear stability analysis of the gravitational instability of magnetized Galactic disks (Hanawa et al. 1992), the gravitational instability is unstable only for the symmetric mode (see also Nakamura et al. 1991). When the GMCs formed by the Parker instability, large-scale colliding clouds were a natural outcome because the clouds slid down along the field lines and accumulated in the valleys of magnetic fields.

This mechanism is also consistent with the suggestion of Elmegreen et al. (1979), who proposed that the Galactic spiral density wave passed through the whole M17 region from northeast to southwest, triggering the star formation in M17-H II. In observations, large-scale colliding flows on the large scale have proven to be an effective way to convert atomic gas to molecular gas and from diffuse gas to dense gas (Nguyen-Luong et al. 2011a, 2011b; Nguyen-Luong et al. 2013; Motte et al. 2014). See also the review on massive star formation in Motte et al. (2018). Sugitani et al. (2019) also pointed out that two gas components with velocities of ∼20 (main) and ∼35 km s^{-1} (secondary) in M17-IRDC could collide. These components can form a broad feature bridge, which is a collection of diffuse gas that has a system velocity between ∼20 km s^{-1} (main) and ∼35 km s^{-1} (Sugitani et al. 2019, S. Kinoshita et al. 2020, in preparation) that is a signature of cloud-cloud-collision, as suggested by numerical simulation of gas kinematics (Inoue & Fukui 2013; Haworth et al. 2015a, 2015b) and by gas kinematic observations (Torii et al. 2011, 2015, 2017, 2018b, 2018a; Fukui et al. 2014, 2016, 2018b, 2018a; Tsuboi et al. 2015; Fujita et al. 2019).

6. Conclusion

We examined the molecular gas structure of the M17 complex using ^{12}CO ($J = 1–0$), ^{13}CO ($J = 1–0$), HCO$^+$ ($J = 1–0$), HCN ($J = 1–0$) and other supplement data. Our main findings are summarized as follows:

1. There are three main molecular clouds with systemic velocities ∼20, 38, and 57 km s^{-1} along the LOS of M17 complex. The main component of 20 km s^{-1} sits in the Sagittarius arm at a distance of ∼2 kpc. The 38 km s^{-1} and 57 km s^{-1} clouds might be associated with Scutum and Norma arms, respectively.
2. The cloud complex can be divided into two clouds: the M17-H II region containing the NGC 6618 star cluster and the M17-IRDC region containing the prominent IRDC network. We confirmed from the molecular observations that M17-H II has a significant fraction of molecular gas (27%) with high column densities and high volume densities that surpass the massive star formation threshold of 1 g cm^{-2}, whereas such high column densities and high volume densities gas are deficient in M17-IRDC (only 0.46%).
3. M17-H II has a higher dense gas fraction than M17-IRDC, as seen in the CMDs of gas column density and the normalized cumulative line luminosity of dense gas tracers such as HCN and HCO$^+$ ($J = 1–0$). Observations

of HCO^+ and HCN emission also confirmed that denser gas is present in the M17-II region than in M17-IRDC.

4. HCO^+ and HCN emission trace all gas with a column density higher than 3×10^{22} cm^{-2} and a higher HCN/HCO^+ ratio in M17-II region might be a good indicator of massive star formation or more evolved evolutionary stages of star formation in M17-II.
5. Applying a Dendrogram analysis to the ^{12}CO data, we identified clumps in the two clouds. Clumps in M17-H II are more compact than those in M17-IRDC and most clumps have virial parameters $\alpha_{vir} <= 1$. On the other hand, most clumps in M17-IRDC have virial parameters $\alpha_{vir} > 1$. Clumps in M17-IRDC need external pressure, while clumps in 17-H II can collapse under their own gravity. Such distinct dynamical states of clumps are consistent with the current activity of star formation, where M17-H II formed massive stars more efficiently in the past, while intense massive star formation has not happened yet in M17-IRDC.
6. The M17 complex appears to have been formed as a whole by large-scale compression. This compression triggered star formation in M17-H II and will trigger star formation in M17-IRDC in the future.

A part of this work was financially supported by JSPS KAKENHI grants No. JP17H02863, JP17H01118, JP26287030, JP17K00963, and JP18H01259. The 45 m radio telescope is operated by NRO, a branch of NAOJ.

Appendix A
Dendrogram Masked Map and Results

Figure 17(a) shows the masked map used to extract sources with Dendrogram, where we masked out all pixels with column density below 3×10^{22} cm^{-2}, and Figure 17(b) shows the detected leaf structures extracted with Dendrogram.

Appendix B
^{12}CO and ^{13}CO ($J = 1$–0) Intensity Maps of the Clouds along the LOS of M17 Complex Integrated in Different Velocity Ranges

We show the ^{12}CO and ^{13}CO ($J = 1$–0) integrated intensities of the observed region integrated over different velocity ranges in Figures 18 and 19, respectively.

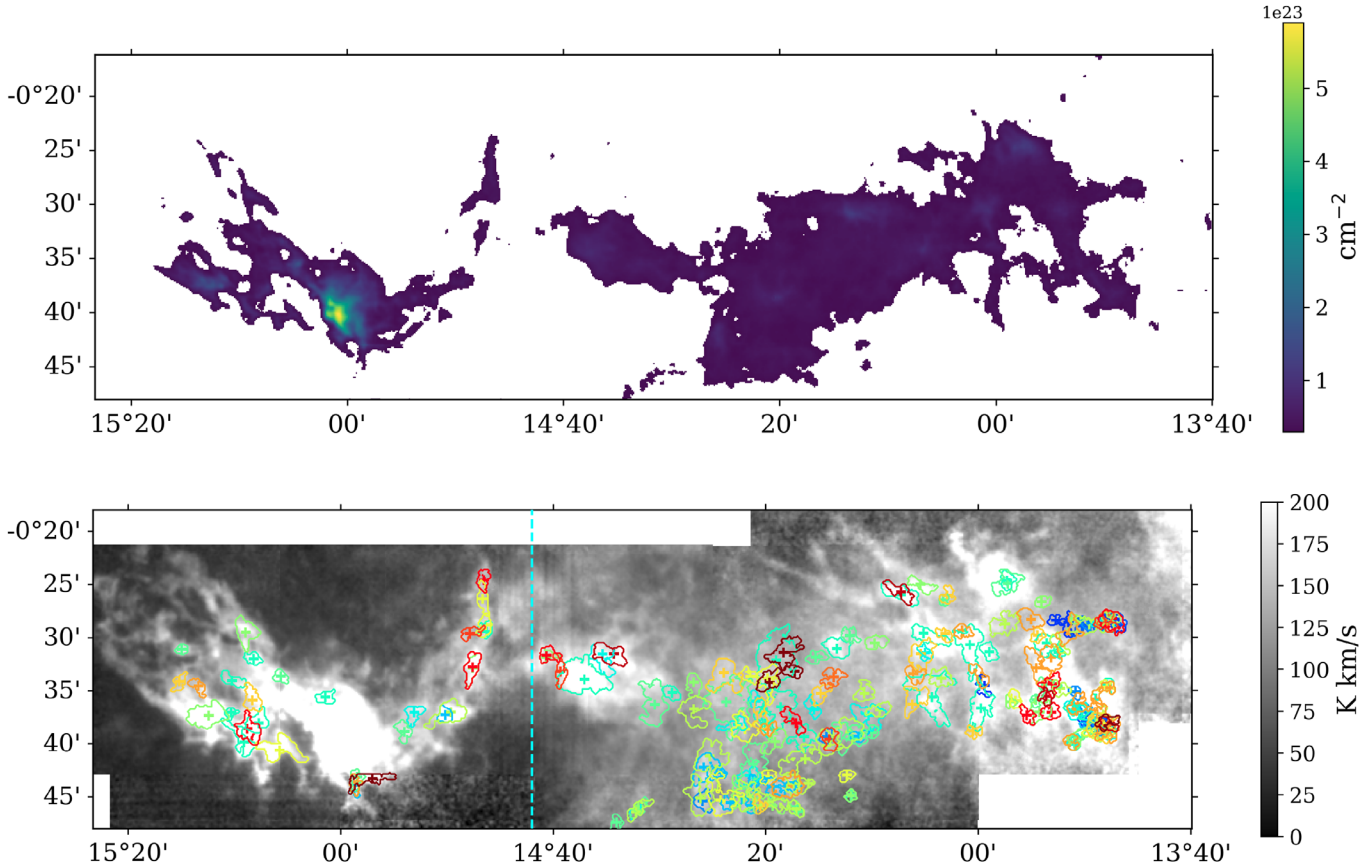

Figure 17. Masked map used to extract sources with Dendrogram, where we masked all pixels with column density below 3×10^{22} cm^{-2} (upper) and the detected leaf structures extracted with the Dendrogram (lower).

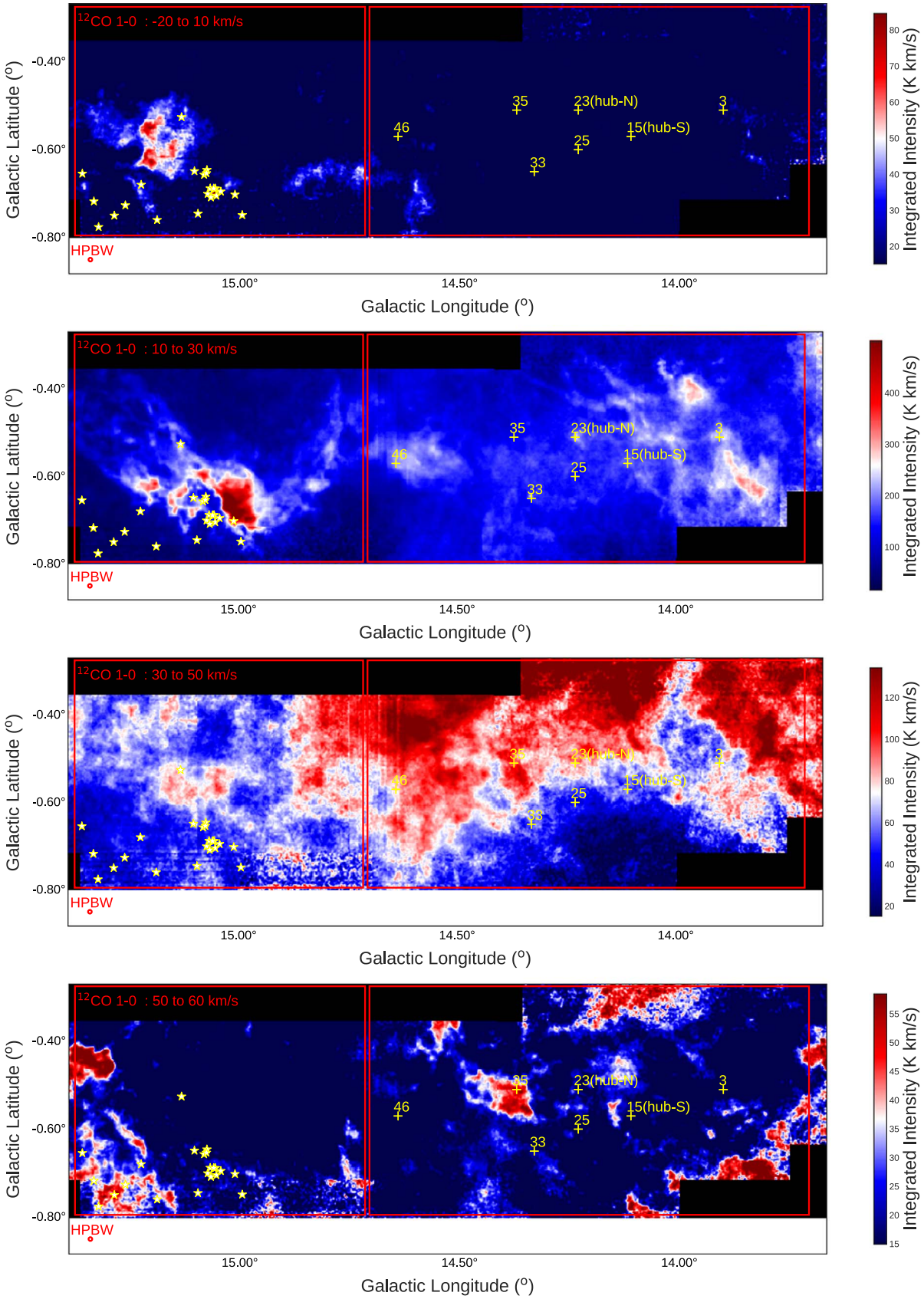

Figure 18. ^{12}CO(J = 1–0) integrated intensity maps of the M17 complex. The velocity range for integration is indicated in the upper left corner of each panel. The red rectangles outline the two prominent star-forming regions: M17-H II (left) and M17-IRDC (right). The star symbols pinpoint the OB star clusters responsible for the giant H II region. The cross symbols pinpoint the locations of the massive cores ($M > 500\ M_{\odot}$) reported by Shimoikura et al. (2019a).

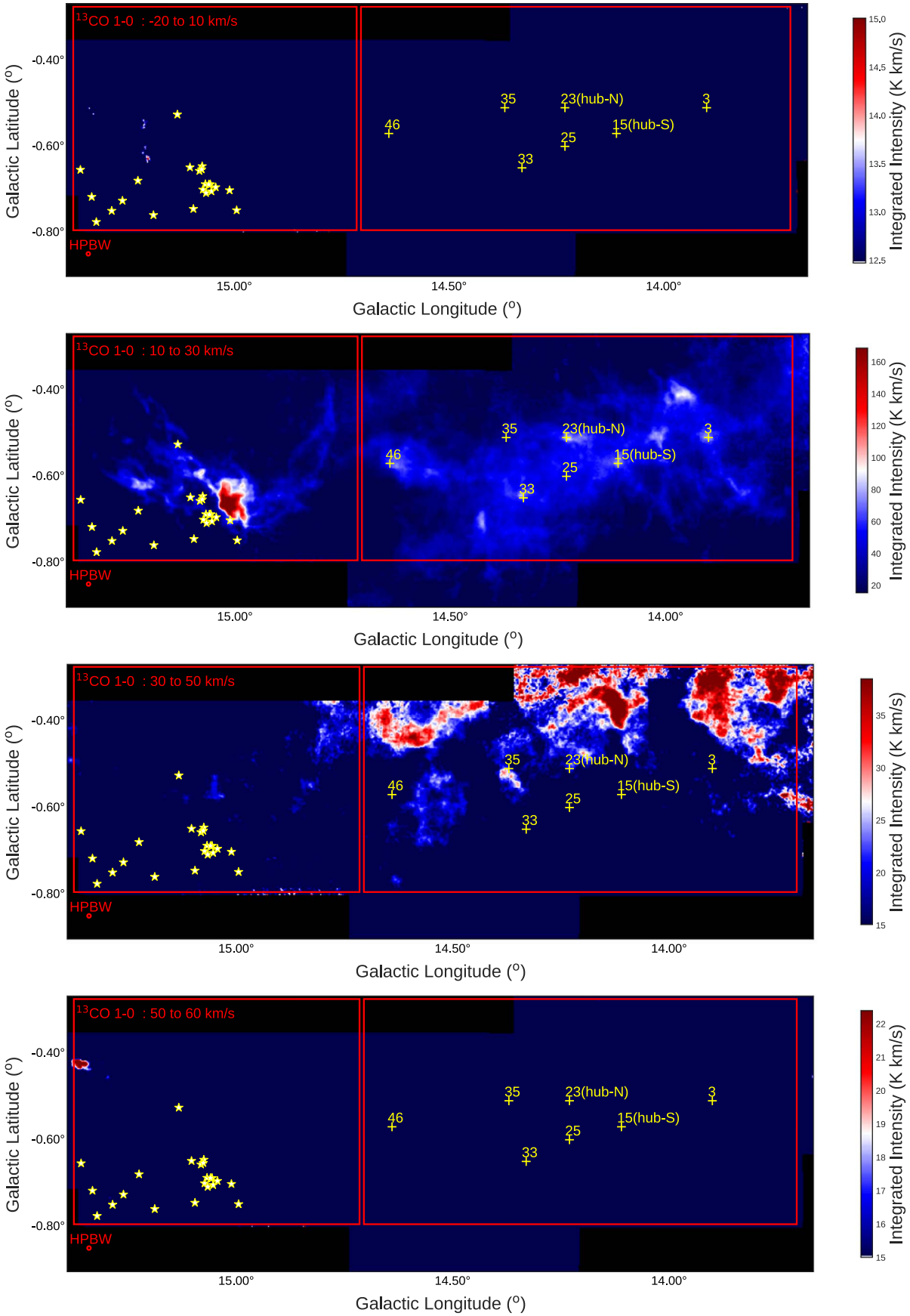

Figure 19. ^{13}CO($J = 1$–0) integrated intensity maps of the M17 complex. The velocity range for integration is indicated in the upper left corner of each panel. The red rectangles outline the two prominent star-forming regions: M17-H II (left) and M17-IRDC (right). The star symbols pinpoint the OB star clusters responsible for the giant H II region. The cross symbols pinpoint the locations of the massive cores ($M > 500\ M_{\odot}$) reported by Shimoikura et al. (2019a).

ORCID iDs

Fumitaka Nakamura https://orcid.org/0000-0001-5431-2294
Koji Sugitani https://orcid.org/0000-0003-3081-6898
Tomomi Shimoikura https://orcid.org/0000-0002-1054-3004
Kazuhito Dobashi https://orcid.org/0000-0001-8058-8577
Kee-Tae Kim https://orcid.org/0000-0003-2412-7092
Patricio Sanhueza https://orcid.org/0000-0002-7125-7685

References

Ando, M., Nagata, T., Sato, S., et al. 2002, ApJ, 574, 187
André, P., Men'shchikov, A., Bontemps, S., et al. 2010, A&A, 518, L102
Arzoumanian, D., André, P., Didelon, P., et al. 2011, A&A, 529, L6
Barnes, P. J., Muller, E., Indermuehle, B., et al. 2015, ApJ, 812, 6
Bertoldi, F., & McKee, C. F. 1992, ApJ, 395, 140
Bolatto, A. D., Wolfire, M., & Leroy, A. K. 2013, ARA&A, 51, 207
Busquet, G., Estalella, R., Palau, A., et al. 2016, ApJ, 819, 139
Carlhoff, P., Nguyen Luong, Q., Schilke, P., et al. 2013, A&A, 560, A24
Chen, H.-R. V., Zhang, Q., Wright, M. C. H., et al. 2019, ApJ, 875, 24
Chibueze, J. O., Kamezaki, T., Omodaka, T., et al. 2016, MNRAS, 460, 1839
Chini, R., Elsaesser, H., & Neckel, T. 1980, A&A, 91, 186
Chira, R.-A., Smith, R. J., Klessen, R. S., Stutz, A. M., & Shetty, R. 2014, MNRAS, 444, 874
Csengeri, T., Bontemps, S., Wyrowski, F., et al. 2017, A&A, 601, A60
Dame, T. M., Hartmann, D., & Thaddeus, P. 2001, ApJ, 547, 792
Dempsey, J. T., Thomas, H. S., & Currie, M. J. 2013, ApJS, 209, 8
Dickman, R. L. 1978, ApJS, 37, 407
Dobashi, K., Shimoikura, T., Endo, N., et al. 2019a, PASJ, 71, S11
Dobashi, K., Shimoikura, T., Katakura, S., Nakamura, F., & Shimajiri, Y. 2019b, PASJ, 71, 12
Elmegreen, B. G. 1989, ApJ, 338, 178
Elmegreen, B. G., Lada, C. J., & Dickinson, D. F. 1979, ApJ, 230, 415
Evans, N. J., II, Heiderman, A., & Vutisalchavakul, N. 2014, ApJ, 782, 114
Field, G. B., Blackman, E. G., & Keto, E. R. 2011, MNRAS, 416, 710
Fujita, S., Torii, K., Kuno, N., et al. 2019, PASJ, in press
Fukui, Y., Ohama, A., Hanaoka, N., et al. 2014, ApJ, 780, 36
Fukui, Y., Ohama, A., Kohno, M., et al. 2018a, PASJ, 70, S46
Fukui, Y., Torii, K., Hattori, Y., et al. 2018b, ApJ, 859, 166
Fukui, Y., Torii, K., Ohama, A., et al. 2016, ApJ, 820, 26
Fuller, G. A., Williams, S. J., & Sridharan, T. K. 2005, A&A, 442, 949
Gao, Y., & Solomon, P. M. 2004, ApJS, 152, 63
Hanawa, T., Matsumoto, R., & Shibata, K. 1992, ApJL, 393, L71
Hanson, M. M., Howarth, I. D., & Conti, P. S. 1997, ApJ, 489, 698
Haworth, T. J., Shima, K., Tasker, E. J., et al. 2015a, MNRAS, 454, 1634
Haworth, T. J., Tasker, E. J., Fukui, Y., et al. 2015b, MNRAS, 450, 10
Heiderman, A., Evans, N. J., II, Allen, L. E., Huard, T., & Heyer, M. 2010, ApJ, 723, 1019
Henkel, C., Wilson, T. L., & Bieging, J. 1982, A&A, 109, 344
Heyer, M., Krawczyk, C., Duval, J., & Jackson, J. M. 2009, ApJ, 699, 1092
Honma, M., Nagayama, T., Ando, K., et al. 2012, PASJ, 64, 136
Inoue, T., & Fukui, Y. 2013, ApJL, 774, L31
Ishii, S., Nakamura, F., Shimajiri, Y., et al. 2019, PASJ, 71, 9
Jiménez-Donaire, M. J., Bigiel, F., Leroy, A. K., et al. 2019, ApJ, 880, 127
Kainulainen, J., Federrath, C., & Henning, T. 2013, A&A, 553, L8
Kauffmann, J., Goldsmith, P. F., Melnick, G., et al. 2017, A&A, 605, L5
Krumholz, M. R., & McKee, C. F. 2008, Natur, 451, 1082
Kuhn, M. A., Getman, K. V., & Feigelson, E. D. 2015, ApJ, 802, 60
Kusune, T., Nakamura, F., Sugitani, K., et al. 2019, PASJ, 71, 5
Lacy, J. H., Sneden, C., Kim, H., & Jaffe, D. T. 2017, ApJ, 838, 66
Lada, C. J., Lombardi, M., & Alves, J. F. 2010, ApJ, 724, 687
Lada, E. A., Bally, J., & Stark, A. A. 1991, ApJ, 368, 432
Langer, W. D., & Penzias, A. A. 1990, ApJ, 357, 477
Mangum, J. G., & Shirley, Y. L. 2015, PASP, 127, 266
Meidt, S. E., Schinnerer, E., García-Burillo, S., et al. 2013, ApJ, 779, 45
Meijerink, R., & Spaans, M. 2005, A&A, 436, 397
Meijerink, R., Spaans, M., & Israel, F. P. 2007, A&A, 461, 793
Minamidani, T., Nishimura, A., Miyamoto, Y., et al. 2016, Proc. SPIE, 9914, 99141Z
Miura, R. E., Espada, D., Hirota, A., et al. 2018, ApJ, 864, 120
Motte, F., Bontemps, S., & Louvet, F. 2018, ARA&A, 56, 41
Motte, F., Nguyên Luong, Q., Schneider, N., et al. 2014, A&A, 571, A32
Nakamura, F., Hanawa, T., & Nakano, T. 1991, PASJ, 43, 685
Nakamura, F., Ishii, S., Dobashi, K., et al. 2019a, PASJ, 71, S3
Nakamura, F., Miura, T., Kitamura, Y., et al. 2012, ApJ, 746, 25
Nakamura, F., Oyamada, S., Okumura, S., et al. 2019b, PASJ, 71, 10
Nguyen-Luong, Q., Motte, F., Carlhoff, P., et al. 2013, ApJ, 775, 88
Nguyen Luong, Q., Motte, F., Hennemann, M., et al. 2011a, A&A, 535, A76
Nguyen Luong, Q., Motte, F., Schuller, F., et al. 2011b, A&A, 529, A41
Nguyen-Luong, Q., Nguyen, H. V. V., Motte, F., et al. 2016, ApJ, 833, 23
Nielbock, M., Chini, R., Jütte, M., & Manthey, E. 2001, A&A, 377, 273
Nishimura, A., Minamidani, T., Umemoto, T., et al. 2018, PASJ, 70, S42
Ohashi, S., Sanhueza, P., Chen, H.-R. V., et al. 2016, ApJ, 833, 209
Papadopoulos, P. P. 2007, ApJ, 656, 792
Parker, E. N. 1966, ApJ, 145, 811
Pety, J., Guzmán, V. V., Orkisz, J. H., et al. 2017, A&A, 599, A98
Povich, M. S., Townsley, L. K., Robitaille, T. P., et al. 2016, ApJ, 825, 125
Povich, M. S., & Whitney, B. A. 2010, ApJL, 714, L285
Rainey, R., White, G. J., Gatley, I., et al. 1987, A&A, 171, 252
Reid, M. J., Dame, T. M., Menten, K. M., & Brunthaler, A. 2016, ApJ, 823, 77
Reid, M. J., Menten, K. M., Brunthaler, A., et al. 2019, ApJ, 885, 131
Rivera-Ingraham, A., Martin, P. G., Polychroni, D., et al. 2015, ApJ, 809, 81
Roberts, H., van der Tak, F. F. S., Fuller, G. A., Plume, R., & Bayet, E. 2011, A&A, 525, A107
Rosolowsky, E. W., Pineda, J. E., Kauffmann, J., & Goodman, A. A. 2008, ApJ, 679, 1338
Sanhueza, P., Contreras, Y., Wu, B., et al. 2019, ApJ, 886, 102
Sanhueza, P., Jackson, J. M., Foster, J. B., et al. 2012, ApJ, 756, 60
Schneider, N., Csengeri, T., Bontemps, S., et al. 2010, A&A, 520, A49
Schuller, F., Beuther, H., Bontemps, S., et al. 2010, Msngr, 141, 20
Scoville, N. Z., Sanders, D. B., & Clemens, D. P. 1986, ApJL, 310, L77
Shibata, K., Nozawa, S., & Matsumoto, R. 1992, PASJ, 44, 265
Shimajiri, Y., André, P., Braine, J., et al. 2017, A&A, 604, A74
Shimoikura, T., Dobashi, K., Hirose, A., et al. 2019a, PASJ, 71, 6
Shimoikura, T., Dobashi, K., Nakamura, F., Shimajiri, Y., & Sugitani, K. 2019b, PASJ, 71, 4
Shirley, Y. L. 2015, PASP, 127, 299
Solomon, P. M., Downes, D., Radford, S. J. E., & Barrett, J. W. 1997, ApJ, 478, 144
Stephens, I. W., Jackson, J. M., Whitaker, J. S., et al. 2016, ApJ, 824, 29
Sugitani, K., Nakamura, F., Shimoikura, T., et al. 2019, PASJ, 71, 7
Tan, J. C. 2000, ApJ, 536, 173
Tanabe, Y., Nakamura, F., Tsukagoshi, T., et al. 2019, PASJ, 71, 8
Torii, K., Enokiya, R., Sano, H., et al. 2011, ApJ, 738, 46
Torii, K., Fujita, S., Matsuo, M., et al. 2018a, PASJ, 70, S51
Torii, K., Hasegawa, K., Hattori, Y., et al. 2015, ApJ, 806, 7
Torii, K., Hattori, Y., Hasegawa, K., et al. 2017, ApJ, 835, 142
Torii, K., Hattori, Y., Matsuo, M., et al. 2018b, PASJ, in press
Townsley, L. K., Feigelson, E. D., Montmerle, T., et al. 2003, ApJ, 593, 874
Tsuboi, M., Miyazaki, A., & Uehara, K. 2015, PASJ, 67, 109
Urquhart, J. S., König, C., Giannetti, A., et al. 2018, MNRAS, 473, 1059
Walker-Smith, S. L., Richer, J. S., Buckle, J. V., Hatchell, J., & Drabek-Maunder, E. 2014, MNRAS, 440, 3568
White, G. J., Phillips, J. P., Beckman, J. E., & Cronin, N. J. 1982, MNRAS, 199, 375
Wienen, M., Wyrowski, F., Menten, K. M., et al. 2015, A&A, 579, A91
Wilson, R. W., Jefferts, K. B., & Penzias, A. A. 1970, ApJL, 161, L43
Wu, B., Tan, J. C., Christie, D., et al. 2017, ApJ, 841, 88
Wu, J., Evans, N. J., II, Shirley, Y. L., & Knez, C. 2010, ApJS, 188, 313
Wu, Y. W., Reid, M. J., Sakai, N., et al. 2019, ApJ, 874, 94
Wu, Y. W., Sato, M., Reid, M. J., et al. 2014, A&A, 566, A17
Xu, Y., Moscadelli, L., Reid, M. J., et al. 2011, ApJ, 733, 25